Estimation of particulate organic carbon export to the ocean from lateral degradations of tropical peatland coasts

Hiroki Kagawa[1], Koichi Yamamoto[1], Sigit Sutikno[2], Muhammad Haidar[3,4], Noerdin Basir[5], Atsushi Koyama[6], Ariyo Kanno[1], Yoshihisa Akamatsu[1], Motoyuki Suzuki[1]

[1]Graduate School of Science and Technology for Innovation, Yamaguchi University, Ube city, Yamaguchi, Japan
[2]Faculty of Engineering, University of Riau, Pekanbaru, Riau province, Indonesia
[3]The Geospatial Information Agency of Indonesia, Jakarta, Indonesia
[4]Institute of Industrial Science, The University of Tokyo, Tokyo, Japan
[5]The state polytechnic of Bengkalis, Bengkalis, Riau province, Indonesia
[6]Faculty of Engineering, University of Miyazaki, Miyazaki city, Miyazaki, Japan

Correspondence to: Koichi Yamamoto (k_yama@yamaguchi-u.ac.jp)

Abstract. Peatlands, which function as long-term carbon sinks, are distributed across subarctic, Arctic, and tropical regions. However, coastal erosion and peat mass movement events (PMMs) are increasingly recognized as significant drivers of peatland degradation, particularly in tropical and permafrost-dominated coastal areas. In the tropics, rapid coastal erosion and PMMs contribute to territorial loss and the export of particulate organic carbon (POC) to the ocean. Similarly, in the Arctic and subarctic regions, coastal retreat and permafrost thaw result in substantial peat loss. The fate of eroded peat whether it remains suspended, settles on the seafloor, or contributes to marine carbon sequestration remains poorly understood. This study quantifies the export of POC and evaluates the extent of peatland degradation due to coastal erosion and PMMs along the northern coast of Bengkalis Island, Indonesia, using field surveys and remote sensing. Between 2017 and 2018, PMMs affected 68 ha, with collapse volumes ranging from 491 m³ to 85,173 m³. UAV-based photogrammetry and cross-sectional topographic surveys revealed elevation losses of 2.01 to 2.07 m over short timescales, triggered by heavy rain and sudden fluctuations in water level. From 2018 to 2021, the rates of coastal erosion varied by land cover type, with erosion in oil palm plantations (3.5 m per 30 days) exceeding that in mangrove and peat swamp forests. The highest recorded rate of 24.8 m per 30 days coincided with high wind speeds and wave activity, emphasizing the role of seasonal climatic forces in peatland degradation. Estimated POC fluxes ranged from 6.35 to 23.9 ktC yr^{-1} due to coastal erosion and 4.45 to 17.1 ktC from PMMs, values 295 to 1,089 times higher than typical riverine POC transport from tropical humid regions. This study identifies a new carbon export pathway from tropical peatland coasts to marine environments. More research is needed to clarify the fate of exported peat, determining whether it remains suspended, settles on the seafloor, or undergoes further degradation.

1 Introduction

Peat is a partially decomposed organic matter that accumulates under conditions such as low temperatures and high humidity, leading to the formation of peatlands. Fig. 1 shows the global distribution of peatlands. These peatlands are distributed across subarctic, arctic, and tropical regions. Throughout the Holocene, peatlands have acted as sustainable carbon sinks, sequestering more than 600 GtC at an average rate exceeding 5 GtC per century (Kleinen et al., 2010; Yu, 2011). The global peatland area has been estimated to range from a minimum of 3,969,831 km² to a maximum of 4,258,068 km², with an intermediate estimate of 3,985,000 km² (Osaki and Tsuji, 2016). The Earth's land area is approximately 13 billion ha (Ministry of the Environment White Paper, 2002), with peatlands accounting for 3.05% to 3.28% of the total land area. Although peatlands cover only about 3% of the Earth's land area, they store approximately 6% of the Earth's total carbon (Page et al., 2011; Scharlemann et al., 2014).

Tropical peatlands are classified into inland peatlands, which typically form in poorly drained inland areas, and coastal peatlands, which develop in marine clays or mangrove sediments within approximately 80 km of the coast (Dommain et al., 2011). The formation of coastal peatlands is closely related to changes in sea level. The rise in sea level after the last ice age resulted in the formation of coastal peatlands, which later evolved into peat domes and inland peatlands around 14,000 years before present (kyBP). Furthermore, the submergence of Sundaland and the emergence of the Java Sea and the Strait of Malacca led to the formation of coastal peatlands when the sea level stabilised between 7,000 and 4,000 years before the present (Dommain et al., 2011). Coastal peatlands are prevalent along the coastlines of Borneo and Sumatra, with 60.1% of Sumatra's coastal peatland area located in Riau Province (Ritung et al., 2011). Tropical peatlands, which occupy 11% of the global peatland area, approximately 56% of the estimated carbon stock of 68.5 Gt in Southeast Asia, Indonesia holds 57.4 Gt of this carbon (Page et al., 2011). However, rapid forest clearing, extensive plantation development and repeated peat fire outbreaks due to drainage have led to substantial carbon emissions, making Indonesian tropical peatlands a global concern (Page et al., 2002; Couwenberg et al., 2010; Hooijer et al., 2010; Frolking et al., 2011). Therefore, Extensive studies on the carbon balance of tropical peatlands, including the biogenic oxidation of peat and other processes, have shown that the seasonality of rainfall, including El Nio-South Oscillation (ENSO) events, significantly affects the carbon balance (Hirano et al., 2007, 2012).

In tropical peatlands, rapid coastal erosion (Fig. 2a) and increased peat mass movement events (PMMs) (Fig. 2b) are of particular concern regarding territorial loss (Fig. 2c) (Sutikno et al., 2017; Yamamoto et al., 2019). Fig. 3 shows a schematic of coastal erosion. Post-erosion coastal topography typically consists of steep cliffs with vegetated areas and the sea immediately adjacent and differentiated by clear boundaries. Additionally, PMMs and peaty debris fan (Evans and Warburton, 2007; Yamamoto et al., 2019) along the coast were identifiable, with clear boundaries demarcated in the hinterland areas of peaty debris fans where land collapses occurred. The coastline in the eroded coastal areas was defined as the opening of a collapsed area abutting a peaty debris fan. In the tropical peatland of Bengkalis Island, Riau Province, Indonesia, research has shown that the decline of the northern coastal mangrove area has led to the exposure of peat deposits along the shoreline. As

a result, three types of erosion and progressive failure mechanisms—toppling failure, rotational sliding, and cantilever failure—are actively occurring, driven by tidal and wave conditions (Basir et al., 2023).

As shown in Fig. 1, peatlands worldwide are widely distributed along coastal areas. Among global peatlands, cases of coastal erosion have been more frequently documented in permafrost-dominated regions (Lantuit et al., 2011; Yunker et al., 1991; Brown et al., 2003; Kreuzburg et al., 2018). In the Arctic, ice-rich coastal areas are particularly vulnerable to erosion. One such site, the Bykovsky Peninsula in northern Siberia, is located along the Lena River Delta (Fig. 1a), extending approximately 150 km along the coastline. Coastal erosion rates in this region have been investigated over a 55-year period (1951–2006) using aerial photographs and satellite imagery, alongside in situ meteorological and tidal data to analyse erosion mechanisms (Lantuit et al., 2011). The results reveal that annual erosion rates exhibit significant interannual and decadal-scale variability. At the Bykovsky Peninsula, sediment accumulation rates reach up to 5.00 m yr^{-1} in certain areas, while the most affected locations experience coastal retreat at rates of up to 10.00 m yr^{-1}. Specifically, the site recorded an average erosion rate of 1.09 m yr^{-1} between 1986 and 2006, while a higher rate of 2.06 m yr^{-1} was observed from 1975 to 1981. The local coastal morphology varies, ranging from relatively stable vegetated slopes to nearly vertical cliffs, with some areas featuring escarpments up to 45 m in height. The geological composition consists of silt, sand, peat, and complex deposits from the Holocene period. Focusing on the summer-to-autumn period in the Arctic (1 June to 15 October, approximately 4.5 per 30 days), storms were defined as events where wind speeds reached 10 m s^{-1} or higher for at least six hours. Based on this definition, 665 storms were recorded between 1958 and 2006, corresponding to an average annual occurrence of approximately 13.6 storms. While storms are often assumed to play a significant role in coastal erosion, no direct correlation has been demonstrated. In permafrost-dominated coastal regions, a "lag effect" (Lantuit and Pollard, 2008) has been identified, where the peak of coastal erosion does not coincide with the peak of storm activity.

Yunker et al., 1991 divided the coastline along the Beaufort Sea from Cape Dalhousie to the Alaska border into 776 coastal segments. For each segment, they calculated the rate of coastal retreat and multiplied it by the thickness of the peat layer to estimate the annual flux of peat material into the Beaufort Sea (Fig. 1b).

At Elson Lagoon, Alaska, a time series of coastal erosion rates along a 10.8 km stretch of the lagoon shoreline was determined by georeferencing aerial photographs and high-resolution satellite imagery from 1949 to 2000 (Fig. 1c). The coastline retreated at an average rate of 0.56 m yr^{-1} from 1948 to 1979, and this rate increased by 47% to 0.86 m yr^{-1} from 1979 to 2000. During this latter period, a total of 28 hectares of land was lost. In the Arctic, coastal erosion is restricted to the ice-free period of approximately 3–4 months yr^{-1}. Along some sections of the Arctic coastline, erosion rates exceeding 10 m yr^{-1} have been recorded, while the regional average ranges from 2 to 6 m yr^{-1} (Rachold et al., 2002). Observations of coastal retreat rates and coastal processes along the Barrow coastline, Alaska, began in the late 1940s and continued into the early 1980s (MacCarthy 1953; Harper 1978; Hume and Schalk 1967; Hume et al., 1972). Harper, 1978 reported that the coastline between Barrow Bay and Peard Bay (a 75 km stretch) experienced an average retreat rate of 0.31 m yr^{-1} from 1949 to 1976. In the Barrow region, permafrost extends to a maximum depth of approximately 400 m, with a thin, peaty surface layer averaging less than 30 cm in thickness (Brown et al., 2003).

The coastal low-lying peatlands along the southern Baltic Sea are estimated to cover an area of approximately 0.16–0.2 km² (Fig. 1d). The offshore boundary of the former peatland roughly coincides with the offshore limit of a dynamic, coast-parallel longshore bar, with peat deposits eroded seaward. Globally, soft coastlines are increasingly affected by adverse processes such as erosion, flooding, and submergence. Sea-level rise and climate change will further intensify the pressure on coastal urban areas and ecosystems, shaping their future development (Vestergaard, 1997; Furmanczyk and Dudzinska-Nowak, 2009). Ongoing coastal dynamic processes, such as wave- and current-induced erosion, sediment transport, and accumulation, have significantly influenced coastline evolution (Lehfeldt and Milbradt, 2000). These processes have led to coastline displacement through land loss or land reclamation, thereby altering the spatial extent of coastal ecosystems and habitats. Among the most vulnerable coastal areas are low-lying coastal wetlands, which face severe threats from saltwater intrusion, erosion, and submergence (Vestergaard, 1997; Nicholls and Cazenave, 2010; Wong et al., 2014). Along the Baltic Sea, approximately 1,800 km² of coastal wetlands are affected by saltwater intrusion (**Sterr, 2008**). In the southern Baltic Sea, coastal erosion has resulted in the loss of approximately 3 km of wetland in an eastward direction since the onset of peatland formation. This has led to peat layer exposure along the beach, where wave erosion occurs along the seaward margin of the wetland following the abrasion of overlying sand layers by storm events.

According to Chambers et al., 2019, the degradation of low-lying coastal wetlands is driven by stressors associated with global climate change and anthropogenic disturbance, leading to losses in both their health and spatial extent. Coastal wetlands are highly vulnerable to sea-level rise, with projections estimating a 22–30% global areal loss by 2100 (Nicholls et al., 1999; IPCC, 2007). Occupying the intertidal ecotone between marine and terrestrial environments, coastal wetlands experience loss from multiple directions. On the seaward edge, storm events, increasing water depth, wave height, and wave power may accelerate erosion (Schwimmer, 2001; Mariotti and Fagherazzi, 2010), while drowning occurs when relative sea-level rise outpaces soil surface elevation gains (Krauss et al., 2010). Additionally, steep topography and human infrastructure may restrict wetlands from migrating upslope, limiting their ability to maintain an optimal elevation relative to sea level. This constraint may result in habitat loss or conversion (Day et al., 2008; Hussein, 2009). Natural wetland degradation drivers include land subsidence, sea-level rise, droughts, hurricanes, tsunamis, storms, erosion, and biological impacts (Dugan, 1993)
.

Malpica-Piñeros et al., 2024 reviewed research activities on Amazonian peatlands, which began with ecological studies in the 1950s. A substantial thematic expansion has been observed since 2009, initially focusing on carbon accumulation and greenhouse gas fluxes, and later shifting toward degradation and conservation after 2017. This trend has been accompanied by a spatial bias favouring the Peruvian lowlands. To date, scientific attention remains limited for the peatlands of western Brazil, the Bolivian lowlands, and the Guianas. Most research on Amazonian peatlands has been conducted by international institutions, but recent years have seen a growing contribution from local research institutes and groups. Amazonia is home to the world's largest tropical rainforest and river system, containing 10% of global species diversity (Charity et al., 2016). Spanning nine countries in tropical South America, the Amazon Basin is primarily situated in Brazil (59%), with the remainder distributed across Bolivia (BOL), Colombia (COL), Ecuador (ECU), French Guiana (GUF), Guyana (GUY), Peru (PER),

Suriname (SUR), and Venezuela (VEN) (Charity et al., 2016). High-altitude peatland landscapes in the Amazon Basin are found across three major regions: the lower Andean Cordillera, the Guiana Shield, and the Brazilian Shield, at elevations between 500 and 1500 m. In Guiana, beach erosion has been reported (Chevallier et al., 2023), indicating a potential for similar coastal processes in this study's context (Fig. 1e).

In boreal peatlands, gully formation due to fluvial erosion is a common process of blanket bog peatland erosion (Evans and Warburton, 2005). In addition to fluvial erosion, peatland failures in boreal peatlands are triggered by snowmelt, rainfall, drainage construction, and peat extraction. Peatland failures have been described using various terms, including peat landslides, bog bursts, and peat failures. However, in Dykes et al., 2007 classified previously documented peatland failures under the broader category of peat mass movements (Fig.1f).

Numerous peatland failures have been reported in northern peatlands such as northern England and Ireland since the 16th century (Bowes et al., 1960; Crisp et al., 1964; Kirk et al., 2001; Mills et al., 2002; Warburton et al., 2004; Dykes et al., 2006; Boylan et al., 2008; Dykes et al., 2011). Peatland failures in northern peatlands are often triggered by heavy or prolonged rainfall (~90 mm in 90 min) (Dykes et al., 2007b). Most failures occur on thin (~2–3 m thick) blanket bog slopes, sometimes involving tens to hundreds of thousands of cubic meters of peat (Dykes et al., 2007). Reported consequences of peatland failures include mass fish kills in river systems (McCahon et al., 1987; Wilson et al., 1996) and disruptions to natural drainage systems (Alexander et al., 1986; Coxon et al., 1989). Peatland failures have been classified based on failure block morphology, soil composition, post-failure topography (e.g., secondary features such as tension cracks), failure mechanisms, peat mass displacement velocity, and moisture content of the failed slope (Dykes et al., 2007). According to this classification, peatland failures are categorized into bog burst, bog flow, bog slide, peat slide, peaty-debris slide, and peat flow (Dykes et al., 2007). According to Boylan et al., 2008, 70 peat slope failures have been reported in Ireland over the past 400 years, although the actual number of occurrences is believed to be significantly higher. Reported cases have increased since 1800, with some failures reaching volumes of up to 5,000,000 m^3, although most are small-scale. A negative correlation between peat thickness and slope angle has been observed, with most failures occurring on slopes between 4° and 8°. However, failures can also occur on steeper slopes (>20°) if the peat layer is thinner, often involving interactions with the underlying mineral soil. Failure zones range from hundreds of meters to several kilometres, and larger failure volumes tend to result in longer peat mass displacement distances

In tropical peatlands, reports of peat mass movements are significantly fewer compared to boreal peatlands. Aside from a recent case on Bengkalis Island (Yamamoto et al., 2019), the only previously documented instance was a suspected peat landslide along the Tutoh River, Malaysia, in 1966 (Wilford, 1966) (Fig. 1h). On Bengkalis Island, coastal landslide has occurred that closely resemble bog bursts observed in boreal peatlands (Dykes et al., 2007). The residual landforms of these bog bursts exhibit crack patterns like those described in progressive failure, a mechanism well known in rock mass collapse, as defined by Bjerrum, 1967.

These lateral degradation processes indicate the export of carbon reservoirs. Furthermore, lateral degradation in coastal areas signifies the export of terrestrial carbon reservoirs to marine environments. A significant portion of this carbon

export to marine environments originates from riverine sources. Riverine carbon fluxes are the main source of terrestrial carbon exports into the ocean, with the annual global export of biogenic organic carbon through from 70 river systems (42.7×10^6 km^2) estimated to be approximately 110–230 MtC (2.58-5.39 tC km^{-2} yr^{-1}) (Galy et al., 2015). The Yellow River has the highest particulate organic carbon (POC) discharge in the world, with a discharge rate of approximately 14.678 tC km^{-2} yr^{-1} (Ludwig et al., 1996), for example. Although few studies have focused on the discharges of organic carbon from the erosion of organic-rich soils, including peatland, the export of POC to the ocean from these soils acts as a global carbon sink (Hilton et al., 2015).

The study by Hedges et al., 1986 demonstrated that most of the organic matter transported by the Amazon River consists of recently biospheric carbon (OC_{recent}) derived from lowland ecosystems. During riverine transport, the oxidation of this dissolved and particulate organic matter releases approximately 500 MtC yr^{-1} into the atmosphere (Richey et al., 2002). Most of this oxidation originates from OC_{recent} and, therefore, does not have a significant impact on the long-term regulation of atmospheric CO_2 (Mayorga et al., 2005). Assuming that CO_2 is emitted from this POC, the resulting CO_2 emissions would correspond to approximately 25 times the total POC flux.

These coastal hazards contribute to lateral carbon transport, as peat particles are exported from coastal areas to the ocean. The ongoing export of peat material from tropical coastal peatlands due to coastal erosion and peat mass movements may have significant implications for the regional carbon budget, particularly if these exports act as a carbon sink in the marine environment. The objective of this study is to assess the extent of peatland degradation caused by coastal erosion and peat mass movement events and to quantify the amount of particulate organic carbon (POC) exported to the ocean due to these lateral degradation processes.

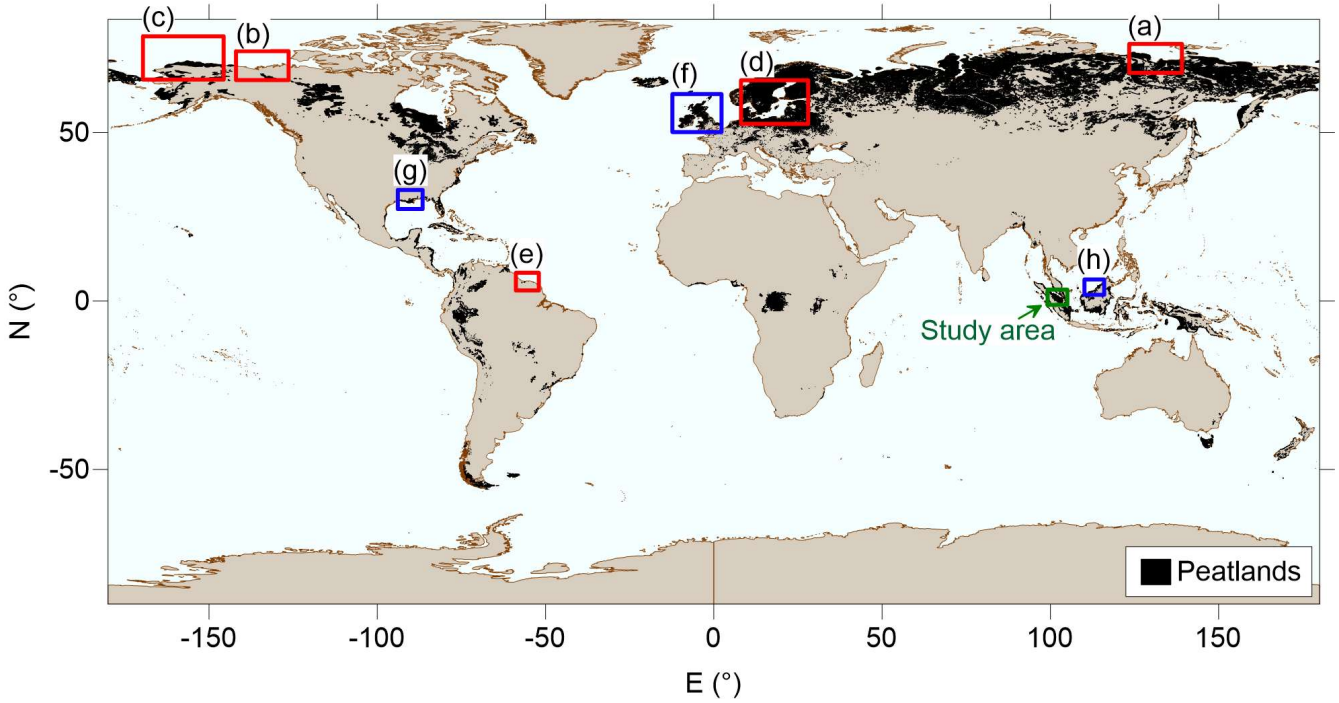

Figure 1: Global Distribution of Peatlands (Based on data from the Global Peatland Database / Greifswald Mire Centre (2024))

190 **Figure 2: Example of lateral degradations in tropical coastal peatland. (a) Coastal erosion (Rangsang Island, Indonesia); (b) Peat mass movement events (Bengkalis Island, Indonesia); (c) Situation where peat is discharged into the ocean due to lateral degradations (Bengkalis Island, Indonesia).**

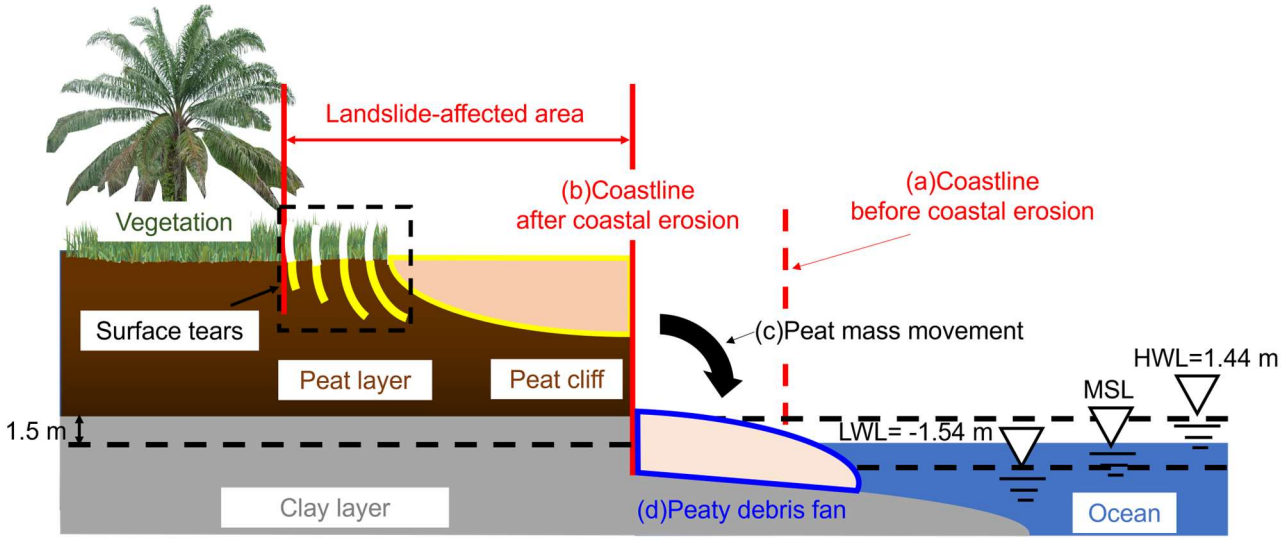

Figure 3: Conceptual figure of costal erosion and PMMs on the peatland coast. Where the High Water Level (HWL) is 1.44 m, the Mean Sea Level (MSL) is 0 m, and the Low Water Level (LWL) is -1.54 m. (a)~(d) show the transitional changes in the coastal landform and a cross-section of the coast. (a) coastline before coastal erosion; (b) coastline after coastal erosion; (c) trace of where PMM occurred; and (d) peaty debris fan formed by peat overhanging the coastline due to the occurrence of PMMs. When PMMs occur, cracks through the peat layer, known as surface tears, appear in the hinterland. In this study, the area affected by the landslide was defined as the hinterland from the peaty debris fan to the head of the source of surface tears. Landslide-affected areas have a thinner vegetation cover.

2 Study area

Bengkalis Island in Riau Province, Indonesia, is a tropical coastal peatland island that encompasses the Straits of Malacca and Bengkalis located 1.6 ° North and 102 ° East, covering an area of approximately 900 km^2 (Fig. 4). Local observations from 2015 to 2018 recorded annual precipitation ranging from 1,381 mm to 2,402 mm. With peat accumulation dating back 5,000 to 6,000 years, the island is characterised by its flat topography and is composed primarily of five peat domes, reaching a maximum elevation between 10 and 15 m above sea level (Supardi et al., 1993). Since 1988, land use trends on the island have changed considerably. In 2019, oil palm plantations had expanded to cover 31.12 % of the island's total area, accompanied by the construction of waterways designed to transport oil palm fruit bunches (Umarhadi et al., 2022).

Currently, the northwest area of Bengkalis Island is experiencing considerable coastal erosion. The coastline gradually approached the highest area of the peat dome on northwest Bengkalis Island. Satellite imagery analysis from 22 December 1988 to 18 July 2013, revealed a coastal erosion rate of approximately 34 m yr^{-1} (Kagawa et al., 2017). Maps created by the U.S. Army Map Service in 1955 documented the presence of mangrove belts on all northern coasts. However, these mangrove

belts cover only a limited area of the northwest coast, revealing the erasure of inland peatland forests facing the sea and the formation of approximately 6 m tall peat cliffs. Furthermore, the island experienced an average subsidence rate of 2.646±1.839 cm yr^{-1} between 2018 and 2019, with the northwestern part recording significant subsidence rates of up to 17.416 cm yr^{-1} due to peat bursts (Umarhadi et al., 2022).

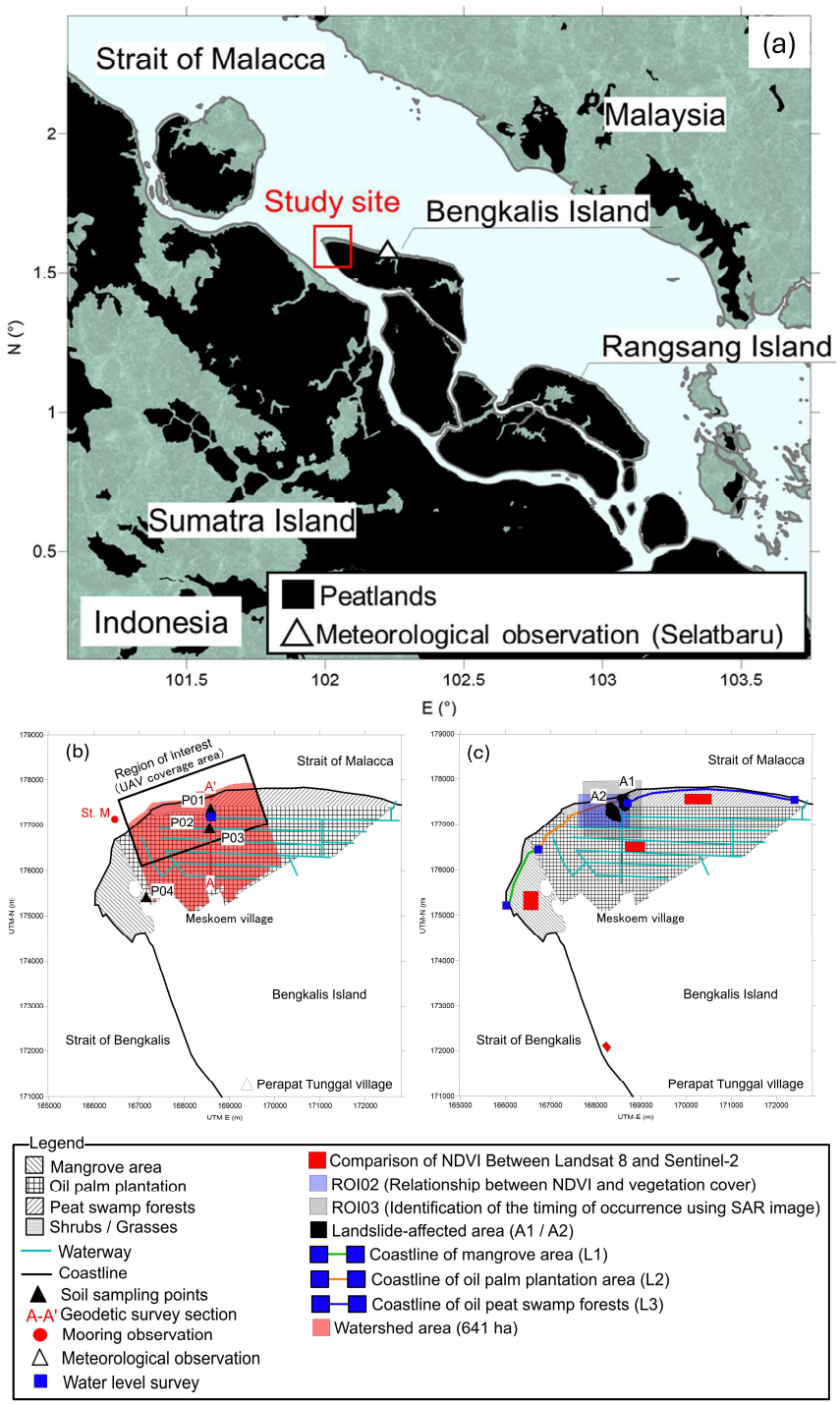

Figure 4: Location of the study site (northwest coast of Bengkalis Island). The peat area is delineated referring to Xu et al., 2017. The northern coast of the island is the area eroded by coastal erosion. The classification of land use is based on field observation.

3 Materials and Methods

The methodology of this study consists of (Fig. 5): (a) To clarify the actual state of PMMs, we identified the timing of their occurrence, (b) To clarify the actual state of coastal erosion, we estimated the coastline retreat, (c) estimation of barren land area using machine classification satellite images, (d) modification of the digital surface model (DSM) to a digital terrain model (DTM), (e) estimation of the POC from the displacement of peat mass caused by PMMs using field surveys and satellite image analyses, and (f) estimation of the POC flux due to coastal erosion using field survey and satellite image analysis. And the meanings of the abbreviations appearing in this study are given in Table 1 and Fig. 6. In this study, multispectral and panchromatic satellite imagery, aerial photogrammetry, DSM data, cross-sectional land surveys and soil sampling were used to assess coastal and peatland degradation. Table 2 lists the images used in this study.

(a) Identification of the timing of peat mass movement events

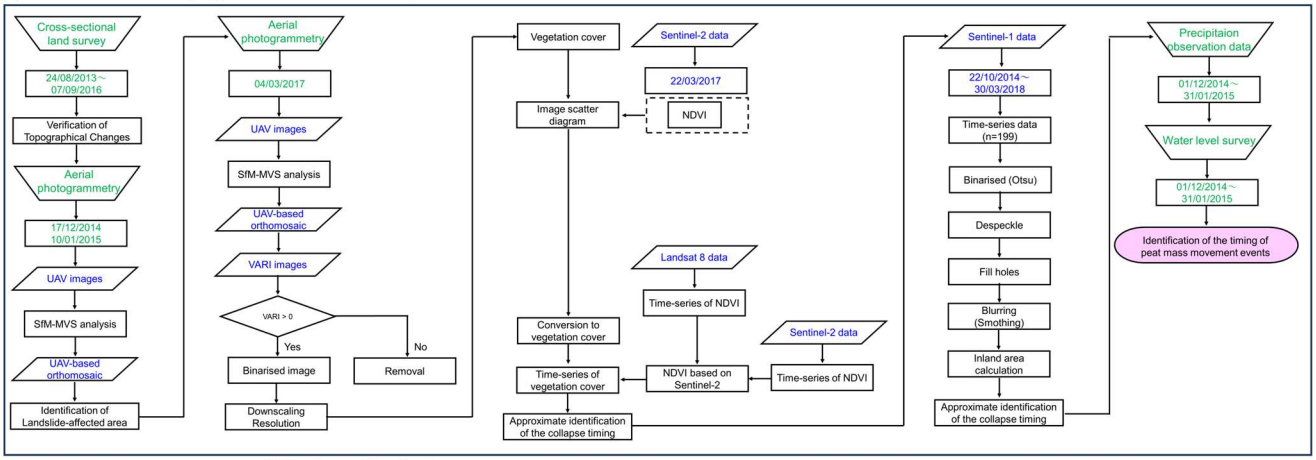

(b) Estimation of coastal retreat

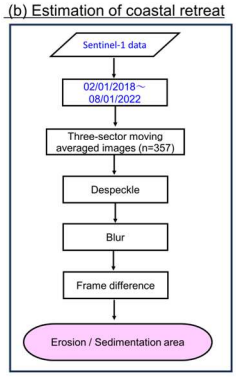

(c) Land cover classification

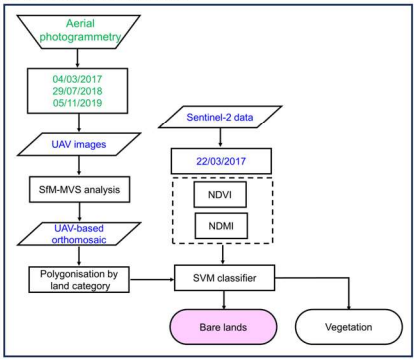

(d) DTM created from DEMNAS

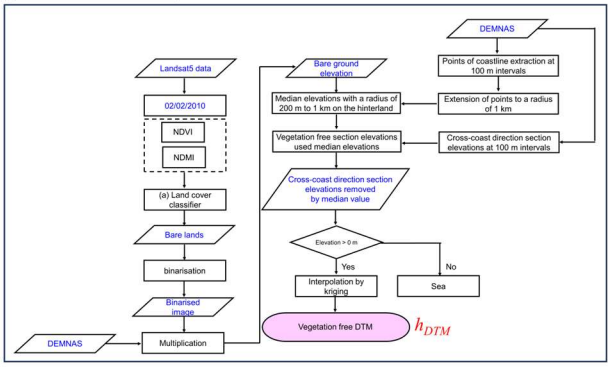

(e) Estimation of the POC from the displacement of peat mass caused by PMMs

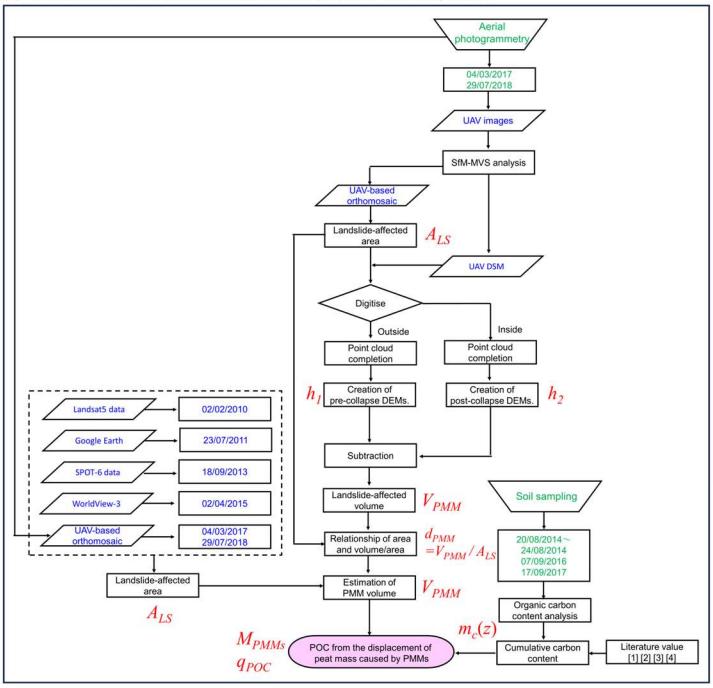

(f) Estimation of POC flux into ocean due to coastal erosion

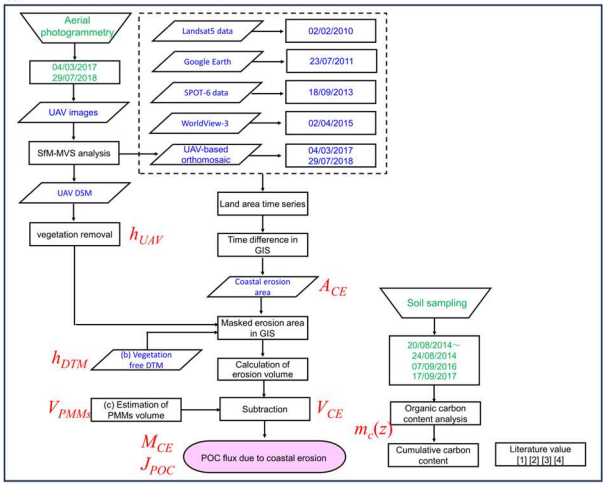

Figure 5: Flow chart used in this study for field surveys and satellite image analysis; (a) To clarify the actual state of PMMs, we identified the timing of their occurrence; (b) To clarify the actual state of coastal erosion, we estimated coastline retreat; (c) an estimation of barren land area by machine classification satellite imaging; (d) the modification of a digital surface model (DSM) to a digital terrain model (DTM).). Abbreviations used: h_{DTM} − Elevation of DTM; (e) and estimation of POC from displacement of peat mass caused by PMMs. Abbreviations used: A_{LS} − Landslide-affected area, h_1 − Elevation before landslide, h_2 − Elevation after landslide, V_{PMM} − Peat mass movement volume, d_{PMM} − Depth of affected by landslide, $m_c(z)$ − Carbon stocks, M_{PMMs} − Mass of POC due to PMMs, q_{POC} − POC fluxes to ocean due to PMMs; (f) an estimation of the POC flux due to coastal erosion; Literature values [1] [2] [3] [4] sourced from Wahyunto et al., 2003; Dariah et al., 2012; Warren et al., 2012 and Rudiyanto et al., 2018. Abbreviations used: h_{UAV} − Elevation of DSM from UAV photogrammetry, A_{CE} − Coastal erosion area, h_{DTM} − Elevation of DTM, V_{PMMs} − Peat mass movements volume, V_{CE} − Coastal erosion volume, $m_c(z)$ − Carbon stocks, M_{CE} − Mass of POC due to coastal erosion, J_{POC} − POC fluxes to ocean due to coastal erosion.

Table 1: Glossary and abbreviations.

Abbreviation	Term	Brief Description
PMM	Peat mass movement	The abbreviation for the term "peat mass movement," which refers to a phenomenon where the ground suddenly collapses and causes landslides due to heavy rainfall or other factors.The areas affected by landslides are characterised by cracks in the surface and peat layers, known as surface tears, which are secondary features located at the head of the landslide zone.
V_{PMM}	Peat mass movement volume	The volume of peat exported to the ocean as a result of a peat mass movement (PMM) event. The loss of the peat volume by a PMM event.
A_{LS}	Landslide-affected area	An area affected by a PMM event, including regions where surface tears, a secondary feature of the collapse, are present.
h_1	Elevation before landslide	The elevation before being affected by a PMM event.
h_2	Elevation after landslide	The elevation after being affected by a PMM event.
V_{PMMs}	Peat mass movements volume	The total volume of peat exported to the ocean as a result of peat mass movement (PMM) events.
V_{CE}	Coastal erosion volume	The total volume of peat exported to the ocean as a result of coastal erosion.
A_{CE}	Coastal erosion area	The area lost as a result of coastal erosion.
h	Elevation of ground before lateral degradation	The elevation before being affected by lateral degradations.
h_B	Thickness of the clay base layer	The thickness of the clay layer, which forms the base layer of peatland coasts.
d_{PMM}	Depth of affected by landslide	The average decline of the elevation by a PMM event, synonymous with V_{PMM}/A_{LS} in this study.
h_{DTM}	Elevation of DTM	The elevation of the ground before coastal erosion and PMMs, specifically the DTM elevation, which is derived from the DEMNAS data.
h_{UAV}	Elevation of DSM from UAV photogrammetry	The elevation of the DSM obtained from UAV photogrammetry, with tree height removed.
z	Peat layer depth from the surface ground	The depth of the peat layer from the surface of the ground in peatland coasts.
$m_c(z)$	Carbon stocks	Carbon stocks as a function of peat depth in peatland coasts.
ρ_d	Dry density of peat	Dry density as a function of peat depth in peatlamd coasts.
α_c	Organic carbon content of peat	Organic carbon as a function of peat depth in peatlamd coasts.
M_{PMM}	Mass of POC due to PMM	The mass of particulate organic carbon (POC) exported to the ocean as a result of a PMM event.
M_{PMMs}	Mass of POC due to PMMs	The mass of particulate organic carbon (POC) exported to the ocean as a result of PMM events.
M_{CE}	Mass of POC due to coastal erosion	The mass of particulate organic carbon (POC) exported to the ocean as a result of coastal erosion.
l	Coastline distance	Coastline distance in the region of interest for each period.
q_{POC}	POC fluxes to ocean due to PMMs	The particulate organic carbon (POC) from the displacement of peat mass caused by PMMs.
J_{POC}	POC fluxes to ocean due to coastal erosion	The particulate organic carbon (POC) fluxes to the ocean due to coastal erosion.
V_{PMM}/A_{LS}	Depth of affected by landslide	The average decline of the elevation by a PMM event, synonymous with d_{PMM} in this study.

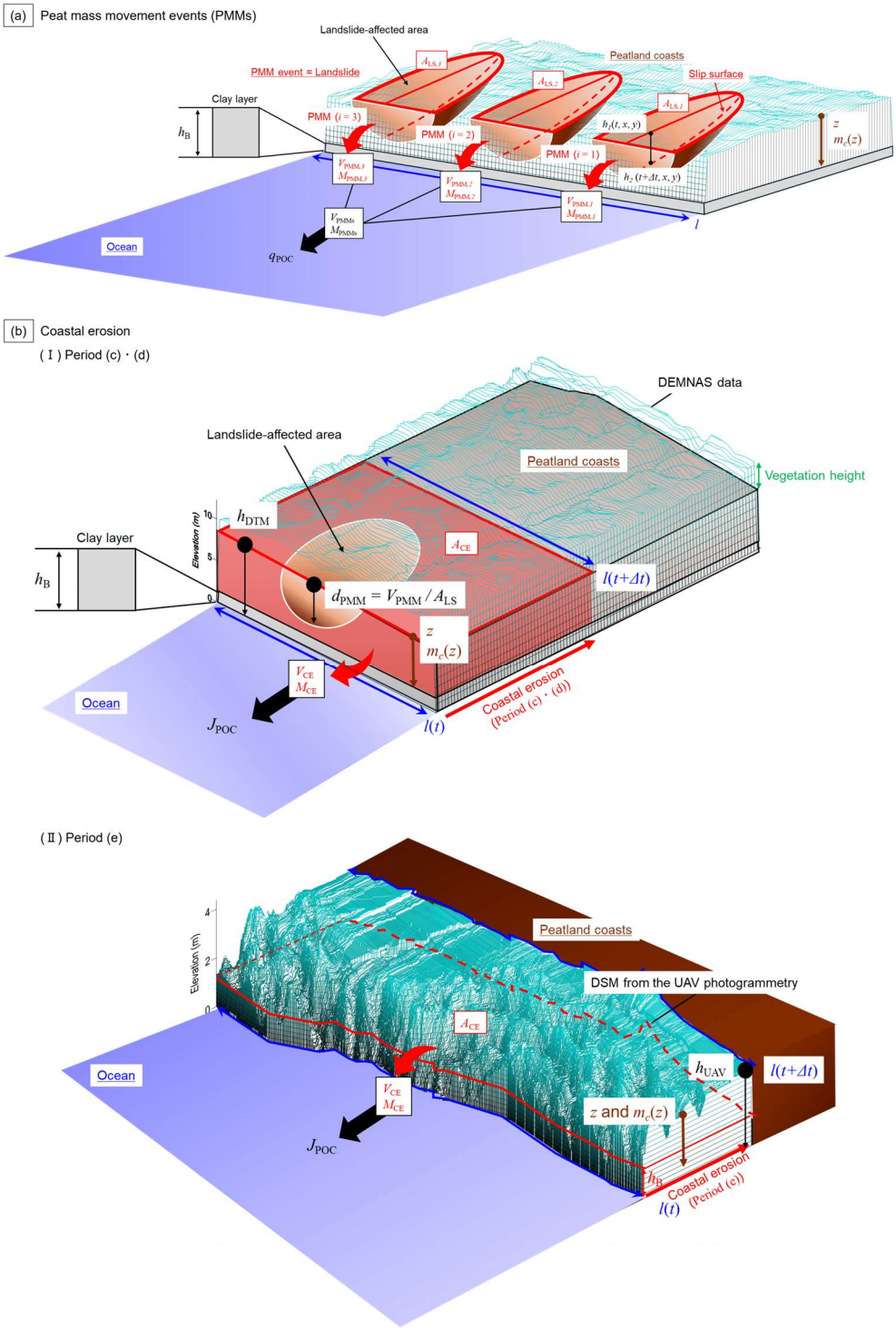

250

Figure 6: Illustrative image of abbreviations. (a) Model of abbreviations associated with peat mass movement events; (b) Model of abbreviations associated with coastal erosion.

Table 2: Remote sensing data used in this study. Satellite imagery data was used in addition to UAV-based orthomosaic and DSM from the aerial photogrammetry results of the field survey.

Image acquisition	Data source	Resolution (m)	Bands used
22/10/2014～30/03/2018 05/01/2018～08/01/2022	Sentinel-1	5×20	C-band
17/12/2014	UAV-based orthomosaic	0.494	-
10/01/2015		0.1	-
5/3/2016		0.086	-
04/03/2017		0.285	-
29/07/2018		1	-
5/11/2019		0.5	-
02/02/2010	Landsat5	30	Red/Green/Blue/NIR/SWIR1
23/07/2011	Google Earth	-	Panchromatic
18/09/2013	SPOT-6	6	Red/Green/Blue
02/04/2015	WorldView-3	1.24	Red/Green/Blue
09/03/2017 03/10/2017～19/02/2022	Landsat8	30	Red/Green/Blue/NIR
22/03/2017 03/10/2017～19/02/2022	Sentinel-2	10	Red/NIR/SWIR1
04/03/2017	UAV DSM	0.285	-
29/07/2018		1	-
2013	DEMNAS	8	X-band/L-band

3.1 Materials

3.1.1 WorldView satellite data and Google Earth image

To identify areas of coastal erosion and PMMs, Google Earth images captured on 23 July 2011 and WorldView-3 multispectral data from 2 April 2015, were used. Launched on 13 August 2014, WorldView-3 operated from a circular sun-synchronous orbit at an altitude of 617 km. WorldView-3 provides eight bands of multispectral data at resolutions of 1.24 (nadir) and 1.38 m (20° off-nadir), and hence a revisit frequency of 4.5 days. Both sensors in the WorldView constellation provide high-resolution Earth observation imagery.

3.1.2 Landsat data

In this study, multispectral Landsat series images, including Landsat 5 Thematic Mapper (TM) and Landsat 8 Operational Land Imager (OLI), were used. Landsat 5 TM images captured on 2 February 2010 were used to delineate coastal erosion and

areas affected by landslides. Additionally, Landsat 5 TM imagery was used to extract bare lands. Landsat 5 TM was launched in March 1984 and carries a Multispectral Scanner Subsystem (MSS) and a TM onboard (USGS and NOAA, 1984). TM has improved the spectral, radiometric, and spatial resolutions relative to MSS. Landsat 8 OLI images from 9 March 2017 to 19 February 2022 were used. Landsat 8 was launched in 2013 and provides high-quality multispectral images at a resolution of 30 m and a revisiting time of 16 days. It aims to provide data continuity to the Landsat Earth observation program, started in the 1970s. These Landsat series data were downloaded from the USGS EarthExplorer (https://earthexplorer.usgs.gov/), and the cloud cover in the collected images was 0%.

3.1.3 Sentinel-1 data

For the identification of the timing of PMM occurrence, Sentinel-1 data acquired from 22 October 2014 to 30 March 2018 were used. In addition, for the estimation of coastal retreat, Sentinel-1 data collected from 5 January 2018 to 8 January 2022 were employed. Sentinel-1 is a constellation of two radar imaging satellites that are part of the European Union's Copernicus Programme. Equipped with C-band synthetic aperture radar (SAR) sensors, Sentinel-1 can capture high-resolution images of the Earth's surface regardless of weather conditions or lighting, making it ideal for continuous monitoring. In its Interferometric Wide swath mode, it offers a resolution of approximately 5×20 m. Its data are used for a variety of applications, including land and ocean monitoring, disaster management, and environmental observation. Data were obtained from USGS EarthExplorer (https://earthexplorer.usgs.gov/).

3.1.4 Sentinel-2 data

Sentinel-2 multispectral imagery captured on 22 March 2017, was used for land cover classification. Sentinel-2B provides 13 bands of multispectral imaging at a resolution of 10 m. Sentinel-2B was launched on 7 March 2017. Part of a European fleet of satellites aimed at delivering core data to the European Commission's Copernicus programme, a programme whose services address six thematic areas: land, marine, atmospheric, climate change, emergency management, and security. In a sun-synchronous orbit at a mean altitude of 786 km above the Earth's surface, MSI samples 13 spectral bands in the visible-near infrared (VNIR) and short-wave infrared (SWIR) spectral range at three different spatial resolutions (10, 20, and 60 m) and allows for a 290 km swath width with a high revisit frequency of 10 days. Data were obtained from USGS EarthExplorer (https://earthexplorer.usgs.gov/).

3.1.4 SPOT-6 data

To elucidate the evolution of PMMs due to coastal erosion, SPOT-6 data captured on 18 September 2013, were used. SPOT-6 provides high-resolution optical images with a resolution of 6 m in multispectral bands. SPOT-6 was launched on 9, September 2012. The satellite is in a nearly circular, sun-synchronous orbit with a period of 98.97 minutes at an altitude of approximately 694 km. SPOT-6 acquires 12-bit data in five spectral bands: blue, green, red, panchromatic, and near-infrared.

3.1.5 DEMNAS (National Digital Elevation Model in Indonesia)

The National Digital Elevation Model in Indonesia (DEMNAS) is a digital surface model (DSM) that was used to create a vegetation-free DTM for the coastal zone in this study. DEMNAS is the result of interpolation from multiple data sources such as IFSAR, TERRASAR-X and ALOS PALSAR at 5 m, 5 m, and 11.25 m resolutions, respectively, with the addition of stereoplotted mass point data in the calculation (EGM2008 vertical datum).

3.1.6 Aerial photogrammetry

To investigate coastal erosion and PMMs, an unmanned aerial vehicle (UAV) was used for aerial photogrammetry. Fig. 4 shows the areas of interest. Table 3 lists the survey schedules, and the equipment used in this study. For photogrammetry, ground control points (GCPs) were established and geolocated using static GNSS measurements (5700/5800, Trimble, USA) or RTK-GNSS (GRX2, Sokkia, Japan). Commercially available software (Photoscan Professional, Agisoft, Russia) was used to process the resulting images for SfM-MVS analysis to create a DSM.

Table 3: Geodetic and aerial photogrammetry survey schedule and equipment.

Year	Month	Geodetic survey	Total length (m)	Aerial photogrammetry survey	Total Area (ha)	Camera
2013	8	✓	740		-	-
2014	3	✓	469		-	-
2014	8	✓	497		-	-
2014	12		-	✓	21	DSLR
2015	1	✓	512	✓	91	DSLR
2015	8	✓	421		-	-
2015	11	✓	304		-	-
2016	3		-	✓	68	DSC
2016	9	✓	399		-	-
2017	3		-	✓	408	DJI Phantom4
2018	7		-	✓	220	DJI Phantom4
2019	11		-	✓	214	DJI Phantom4

3.1.7 Cross-sectional land survey

To examine changes in the cross-sectional profile of the land, particularly in the plantation in Meskom Village, a survey was carried out along a north–south transect (Section A-A'). Fig. 4 displays the transect and Table 3 lists the survey schedules. A Sokkia GRX2 RTK-GNSS system based on reference points located in the Bengkalis state polytechnic was used to perform the measurements.

3.1.8 Sampling and analysis of peat soils

Soil sampling was performed to determine the organic carbon content of the peat soil. Fig. 4 shows the sampling points and Table 4 lists the sampling and analysis information. A Dutch-style peat sampler (DIK-105A, Daiki Rika Kogyo Co., Ltd.,

Saitama, Japan) was used to extract samples up to 6 m below the clay layer. Quantitative sampling was performed to measure the density at the time of collection. The samples were dried at 105 ° C and the organic carbon and nitrogen content was analysed using a CHN analyser (JM-10 analyser, J-Science Lab., Kyoto, Japan).

Table 4: Details of the sampling and analysis of peat soil.

No.	Coordinates		Date	Depth (cm)	Layers (50 cm)	Land use	Analysis items
	Latitude	Longitude					
P01	1.6019°N	102.0218°E	20 - 24/08/2014	600	12	Oil palm plantation	Moisture content, Dry density, Carbon content
P02	1.6025°N	102.0218°E	20 - 24/08/2014	600	12	Oil palm plantation	Moisture content, Dry density, Carbon content
P03	1.5987°N	102.0216°E	17/09/2017	167	4	Oil palm plantation	Moisture content, Dry density, Carbon content
P04	1.5849°N	102.0090°E	07/09/2016	294	6	Oil palm plantation	Moisture content, Dry density, Carbon content

3.1.9 Mooring observations

From 4 November 2019 to 13 January 2020, a pressure-type memory wave gauge (INFINITY-CTW) was moored approximately 500 m offshore from a coast undergoing significant erosion to measure wave heights from the temporal variation in pressure (Fig. 4 St.M). Based on these measurements, significant wave heights were calculated for every two-hour interval.

3.1.10 Meteorological observations

To elucidate the temporal characteristics of PMMs occurrences and the features of coastal erosion, meteorological observation instruments were installed at Selatbaru and Perapat Tunggal on Bunkaris Island (Fig. 4), and measurements were conducted. The instruments used were the SESAME II-05d (Midori Engineering Institute). This study utilized data collected from 2014 to 2021.

3.1.11 Water level survey

To investigate changes in water levels within channels in areas where peat collapse occurs frequently, a water level gauge was installed at the location shown in Fig. 4. A monitoring well was constructed at the measurement site using a polyvinyl chloride (PVC) pipe, and the channel water level was recorded using a HOBO U-20 water level logger. This study utilized data collected from 1 December 2014 to 31 January 2015.

3.2 Methods

3.2.1 Time series of NDVI data viewed and analysed in Sentinel hub EO browser

EO Browser was utilized as a web-based platform for processing remote sensing data in a cloud computing environment. Sentinel images were obtained from Sentinel Hub, which is connected to EO Browser via API, and statistical analysis of the

Normalized Difference Vegetation Index (NDVI) was conducted within EO Browser. The procedure for NDVI statistical analysis in EO Browser is as follows: First, the acquisition period for the Sentinel images was selected, and polygons from a KML file created in a GIS environment were imported into EO Browser. The statistical analysis of NDVI allowed for the calculation of average values within the selected polygons and the assessment of temporal changes over the specified period. To minimize the impact of cloud cover, the analysis was conducted with cloud coverage set to 0%. Since erroneous data were occasionally included, the exported CSV files were reviewed, and any erroneous data were manually removed.

3.2.2 Relationship between NDVI and vegetation cover

Time-series changes in NDVI were analyzed using Landsat8, while Sentinel-2 imagery was employed to examine the relationship between NDVI and vegetation cover. Consequently, we first established the relationship between NDVI values from Landsat8 and Sentinel-2. An oil palm plantation was selected as the target for comparison (Fig. 4c). To determine whether NDVI variation is related to vegetation coverage, VARI (Visible Atmospherically Resistant Index) images were generated from UAV aerial photogrammetric data acquired on 4 March 2017. The VARI images were binarized using a threshold of 0, and a scatter diagram was constructed to compare the binarized VARI values with the NDVI data. Pixel sizes were matched to facilitate the correlation analysis between vegetation coverage and NDVI. NDVI (Landsat 8), NDVI (Sentinel-2) and VARI were calculated using Eq. (1), Eq. (2) and Eq. (3).

$$NDVI = \frac{B5-B4}{B5+B4} \quad (1)$$

$$NDVI = \frac{B8-B4}{B8+B4} \quad (2)$$

$$VARI = \frac{G-R}{G+R-B} \quad (3)$$

Where *B5* represents the NIR with 30 m resolution (wavelength: 850-880 nm); *B4* represents the red band with 30 m resolution (wavelength: 640-670 nm); *B8* represents the NIR with 10 m resolution (wavelength: 842 nm); *B4* represents the red band with 10 m resolution (wavelength: 665 nm). *G* represents the green band; *R* represents the red band; *B* represents the blue band.

3.2.3 Identification of the timing of PMM occurrence using SAR image

Changes in the land area within the landslide-affected areas were analysed using Sentinel-1 SAR images acquired between 22 October 2014 and 30 March 2018. The time-series data were downloaded as an animated GIF from the EO Browser, and the region of interest is shown in Fig. 4. The image analysis procedure involved applying a moving average over three consecutive acquisition intervals and smoothing the coastline using a blurring technique. Subsequently, noise within the region of interest was removed. After blurring, the images were binarized to isolate the land areas, thereby revealing changes in the extracted region. The expansion of this area a characteristic feature of peaty debris fans occurs following peat mass movement events.

3.2.4 Estimation of coastal retreat using SAR image

Using 359 Sentinel-1 SAR images acquired from 5 January 2018 to 8 January 2022, the average cumulative coastline retreat was calculated for each land cover type namely, the mangrove belt, oil palm plantation, and peat swamp forest. The specific coastlines corresponding to these land cover types are shown in Fig. 4, and the analytical workflow is illustrated in Fig. 5.

The analysis procedure was as follows. First, a moving average was applied over three consecutive acquisition intervals (including the day before and after each image) to smooth the data. Next, the coastline and land areas were separated by binarization. Noise reduction was then performed, and the difference between consecutive images was computed to extract the regions undergoing coastline changes. The area of these regions was calculated, and by dividing the computed area by the corresponding coastline length for each land cover type, the average coastline retreat was determined.

For 2018 and 2021, local observations (Fig. 4) of precipitation and wind speed were summarized as annual precipitation and annual maximum wind speed. Furthermore, the relationship between significant wave height and maximum wind speed was examined for the period from 4 November 2019 to 13 January 2020 using data from mooring observations. In analysing maximum wind speed, data recorded at Selatbaru were used; since the moored observation points differed, a moving average covering two hours before and after each observation was applied to better represent the relationship between significant wave height and maximum wind speed.

Additionally, annual wind roses were generated using 10-minute interval observations of maximum wind speed and direction recorded at Selatbaru and Perapat Tunggal in 2018 and 2021. These combined meteorological and remote sensing analyses allowed for a comprehensive discussion of coastal erosion characteristics across different land cover types.

3.2.5 Land cover classification using machine learning

To extract bare land from oil palm plantations in satellite images, we used the normalised difference vegetation index (NDVI) and the normalised difference moisture index (NDMI) derived from Sentinel-2 imagery to classify the land cover. NDVI and NDMI were calculated using Eq. (2) and Eq. (4), respectively. For machine learning, Support Vector Machine (SVM) algorithms were used to classify the oil palm tree plantations from the other landcovers. The UAV images, taken on 4 March 2017, 29 July 2018, and 5 November 2019, were used as the ground truth of the land cover. The precision of the land cover classification was evaluated by calculating the true positive rate, recall, specificity, precision, negative predictive value and F-score based on the confusion matrix. The dividing lines were calculated with palm oil plantation vegetation as true positives (TP) and other types of land cover as false negatives (FN).

$$NDMI = \frac{B8A - B11}{B8A + B1} \quad (4)$$

Where *B8A* represents the NIR with 20 m resolution (wavelength: 865 nm); *B11* represents the SWIR with 20 m resolution (wavelength: 1610 nm). According to Mandanici and Bitelli, 2016, the Pearson correlation coefficient and the slope of the linear relationship between the reflectance and index values of the multispectral instrument (MSI) and the TM5 bands are as

close to 1 as possible, with the intercept close to 0. Therefore, the machine learning model for land cover classification created for Sentinel-2 images was applied directly to Landsat5 images.

3.2.6 Vegetation removal from DEMNAS data

Because DEMNAS is a DSM that contains the tree height (vegetation), we removed the tree height from the DSM to make DTM. First, the bare lands in the research area in Landsat 5 image taken on 2 February 2010 were identified by the classifier that was established in 3.2.1 and binarized. The binarized bare land area and DEMNAS data were combined to extract elevation values for bare land. During this process, the peat swamp forest and adjacent bare road and a radius of 200 m from the coastline that were flagged as anomalies were masked (Fig. 7a). The 200 m radius DEMNAS data depicted collapsed terrain, which would not need to remove tree heights; therefore, these areas were excised. The DEMNAS derived coastline, which the points of the altitudes of 0 m at 100 m intervals were extracted (Fig. 7b). An approximation of the polynomial curve of the extracted coastline was calculated and a 2 km offshore measurement line was constructed centred on the coast (Fig. 7c). The radius of 1 km from the coastline was set as a buffer area for buffer analyses in GIS to obtain elevation of the bare land (Figs. 7d and 7e). For any point in which statistical values were not attainable, linear interpolation was applied between adjacent points. The elevation difference from the median bare land elevation was considered as tree heights and the difference was subtracted to calculate the bare land elevation. Values above 0 m elevation were used to interpolate by kriging to generate a DTM with an 8 m resolution.

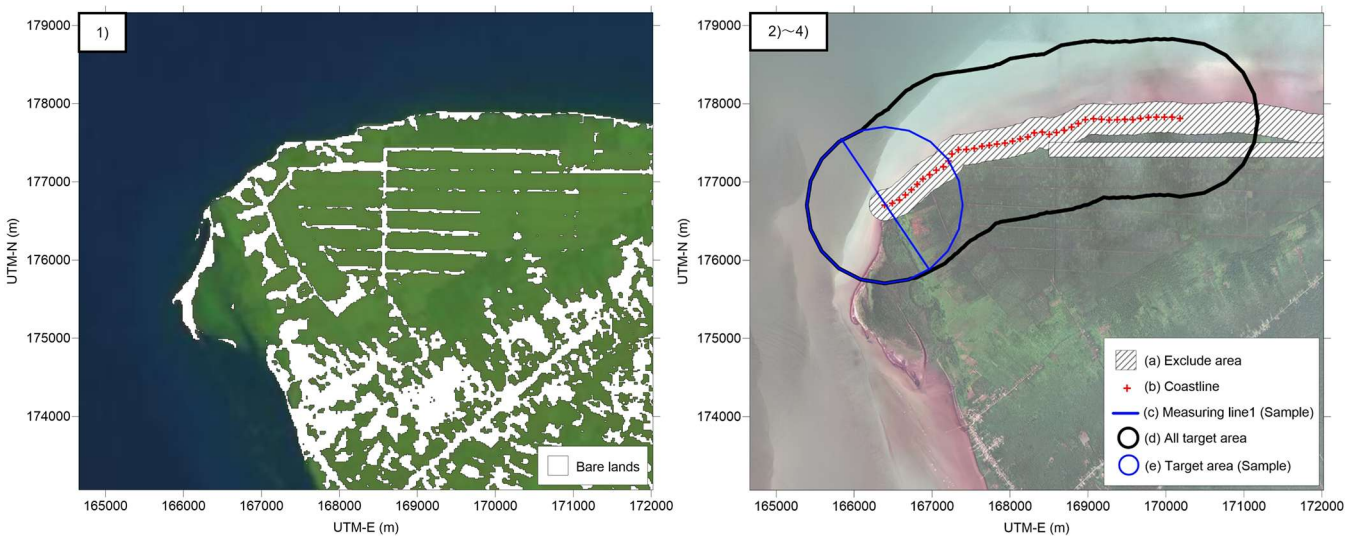

Figure 7: Methodology of removal of vegetation from DEMNAS data. 1) A Landsat5 image (2 February 2010) was used to classify bare land and other land covers using machine learning. 2) The bare land raster was set at 1 and multiplied by the DEMNAS data to produce the bare land elevation data. The elevation anomalies at the boundary between the peat swamp forest and the bare road and a radius of 200 m from the coastline (a) were masked. 3) A measuring line was made in the offshore direction from inland at

points where the coastline was divided at 100 m intervals (b) (c). 4) The median elevation of the bare lands located 1 km (d) (e) from the coastline was assigned to the coastline and linearly complemented.

3.2.7 Estimation of the volume of exported land slide-induced peat to the ocean

Aerial photogrammetry-derived DSMs were used to establish the relationship between the area and the loss of the peat volume by PMMs. This relationship was then used to estimate the losses in peat volume in areas affected by landslides identified in multispectral satellite imagery. Elevations before and after collapse were obtained by manually digitising the edges and inside the landslide-affected area within the GIS software (QGIS ver. 3.20) using orthomosaics and DSMs resulting from aerial photogrammetry carried out on 4 March 2017 and 29 July 2018, respectively, and within Estimation of the volume of export of land slide-induced peat to the ocean (Figs. A1g, A1h). The landslide-affected areas were judged by the characteristics of the ground, such as surface tension cracks or the presence of peat blocks. Tension cracks and irregular peat blocks are some of the characteristic features of peat mass movements (Warburton et al., 2004). Two digital elevation models (DEMs) were generated using aerial photogrammetry results. The first DEM was the initial land surface, which was recreated by interpolation using elevations of the points extracted from the edges of the areas affected by landslides within the DSM (Fig. A1g). The second DEM was the post-collapse DEM, which were generated by sampling elevation data in areas affected by landslides in the vegetation removed DSM (Figs. A1f, A1h and A1i). The volume of peat exported to the sea due to collapse was deduced by calculating the difference between the first DEM and the second DEM. The method to calculate the volume of peat exported by a PMM event is expressed in Eq. (5),

$$V_{\mathrm{PMM},i} = \iint_{A_{\mathrm{LS},i}} \big(h_1(t,x,y) - h_2(t+\Delta t,x,y)\big)dxdy \quad (5)$$

where $V_{\mathrm{PMM},\,i}$ represents the volume of peat exported to the ocean by a PMM event i (m^3), $A_{\mathrm{LS},\,i}$ represents the area i affected by the landslide (m^2), h_1 represents the elevation before the landslide (m), h_2 represents the elevation after the landslide (m), x and y represent the distance (m), t represents the change in time.

3.2.8 Estimation of the volume of peat exported by the PMMs using optical satellite images and UAV-based orthomosaic

Landslide-affected areas were extracted from optical satellite images and orthomosaic based on UAVs (Fig. A1a, A1b, A1c, A1d and A1e). When landslide-affected areas were extracted from multispectral satellite imagery, areas with sparse vegetation were spotted using the true colour image and the false colour image (Figs. A1a, A1b, A1c, and A1d). The volumes of peat exported by landslide were estimated in these areas based on a previously determined area–volume/area relationship. Landslide-affected area: $A_{\mathrm{LS},i}$ calculation was performed in the GIS software. The total amount exported to the ocean by PMMs: the V_{PMMs} are shown in Eq. (6) and Eq. (7).

$$V_{\mathrm{PMMs}} = \sum V_{\mathrm{PMM},i} \quad (6)$$

$$V_{\mathrm{PMMs}} = \sum f\big(A_{\mathrm{LS},i}\big) \quad (7)$$

where $A_{LS,i}$ represents the area i affected by the landslide (m^2). f represents a function to estimate the volume of the Landslide-affected area. This study considered traced errors in landslide-affected areas, which were calculated by manual tracing in GIS software (Fig. B). We evaluated the errors caused by differences in resolution using satellite images from Landsat 8 and Sentinel-2 acquired at the same time (n=7). To achieve this, we conducted 20 tracings per time for comparison (Fig. C).

3.2.9 Calculation of coastal erosion volume

To elucidate the area and volumetric magnitude of peatland loss due to coastal erosion, we drew coastlines using GIS software (QGIS 3.10) based on satellite images, orthomosaic results from aerial photogrammetry, and analysed their temporal changes.es. The defining equation to calculate coastal erosion is shown in Eq. (8).

$$V_{CE} = \iint_{A_{CE}} (h(x,y) - h_B(x,y) - d_{PMM}(x,y))dxdy \quad (8)$$

where V_{CE} represents the volume of peat exported by coastal erosion in each period (m^3), h represents the elevation of the ground before coastal erosion and PMMs (m), h_B represents the thickness of the clay base layer (m), A_{CE} represents the area eroded by coastal erosion (m^2) and d_{PMM} represents the average elevation drop by a PMM event (m). d_{PMM} is described by the following Eq. (9).

$$d_{PMM} = \frac{V_{PMM}}{A_{LS}} \quad (9)$$

where V_{PMM} represents the volume of peat exported to the ocean by a PMM event (m^3), and A_{LS} represents the landslide-affected area (m^2).

Multispectral satellite imagery from Table 2 and orthomosaic results from aerial photogrammetry were used to plot the coastlines. For period (c), from 18 September 2013 to 2 April 2015, and (d) from 2 April 2015 to 4 March 2017, the ground elevations before the erosion were determined using the DTM derived from the DEMNAS data. During period (e), spanning from 4 March 2017 to 29 July 2018, perversion ground elevations were obtained from a DSM generated using aerial photogrammetry results obtained from the UAV. The DSM of the UAV photogrammetry was adjusted to remove the height of the tree prior to use. The process of excluding tree heights from the DSM was carried out by checking trees on a UAV-based orthomosaic. Furthermore, the DSM of the UAV was corrected using the root mean square error (RMSE) values of the DTM generated from the RTK-GNSS and DEMNAS data. DTM using DEMNAS data does not consider landslide-affected areas, so landslide volumes are subtracted, but DSM from aerial photogrammetry results reflect spilt volumes due to landslides, so landslide volumes were used as they are, without subtraction. The volume of peat exported by coastal erosion, estimated using DTM, and the volume of peat exported by coastal erosion, estimated using DSM from UAV photogrammetry, are shown in the Eq. (10).

$$V_{CE} = \begin{cases} \iint_{A_{CE}} \left(h_{DTM}(x,y) - h_B(x,y) - d_{PMM}(x,y)\right)dxdy & (h = h_{DTM}) \\ \iint_{A_{CE}} \left(h_{UAV}(x,y) - h_B(x,y)\right)dxdy & (h = h_{UAV}) \end{cases} \quad (10)$$

where V_{CE} represents the volume of peat exported by coastal erosion in each period (m^3), h_{DTM} represents the elevation of the ground before coastal erosion and PMMs, that is, the elevation of DTM (m), h_B represents the thickness of the clay base layer (m), A_{CE} represents the area eroded by coastal erosion (m^2), and d_{PMM} represents the average decrease in elevation due to a PMM event (m). h_{UAV} represents the elevation of the vegetation-free DSM based on the UAV photogrammetry (m). This study considered traced errors in coastal erosion areas, which were calculated by manual tracing in GIS software (Fig. B).

3.2.10 Estimation of POC mass by PMM event and estimation of POC flux due to coastal erosions

The mass of the POC by the displacement of peat mass caused by PMMs and the POC flux due to coastal erosions were calculated by the spatial distributions of the loss of the peat volume and depth-dependent carbon stock of the peat. The carbon stock of peat $m_c(z)$ (t m^{-2}) until the depth z (m) of the peat from the surface of the ground was calculated using the following Eq. (11),

$$m_c(z) = \int_0^z \rho_d \alpha_c dz \tag{11}$$

where ρ_d represents the dry density (t m^{-3}) and α_c represents the organic carbon content (-). They were combined from the results of field surveys with the value of the literature obtained from Wahyunto et al., 2003; Dariah et al., 2012; Warren et al., 2012 and Rudiyanto et al., 2018.

The mass of POC caused by a PMM event was calculated using Eq. (12),

$$M_{PMM} = m_c(d_{PMM})A_{LS} \tag{12}$$

where M_{PMM} (tC) represents the mass of POC, the variable d_{PMM} represents the average decrease of elevation by a PMM event (m), and A_{LS} represents landslide-affected area (m^2). The amount of POC exported by the PMMs (tC) in each period was calculated using the Eq. (13),

$$M_{PMMs} = \sum M_{PMM} \tag{13}$$

where M_{PMMs} (tC) represent the mass of POC exported by the PMMs in each period. The mass of POC which is exported to the ocean caused by coastal erosion in each period was calculated using the Eq. (14). Eq. (14) is divided into two cases for elevation h (m) before coastal erosion and a PMM event: the case using DTM and the case using UAV aerial photogrammetry results.

$$M_{CE} = \begin{cases} \iint_{A_{CE}} m_c\big(h_{DTM}(x,y) - h_B(x,y) - d_{PMM}(x,y)\big)dxdy & (h = h_{DTM}) \\ \iint_{A_{CE}} m_c\big(h_{UAV}(x,y) - h_B(x,y)\big)dxdy & (h = h_{UAV}) \end{cases} \tag{14}$$

where M_{CE} represents the mass of POC caused by coastal erosion (tC), h_{DTM} represents the elevation of the ground before coastal erosion and PMMs, i.e. the elevation of the DTM (m), h_B represents the thickness of the clay base layer (m), A_{CE} represents the eroded area by coastal erosion (m^2) and d_{PMM} represents the average decline of the elevation by a PMM event (m), and h_{UAV} represents the elevation of the DSM from the UAV photogrammetry was removed tree height (m). The POC from the displacement of peat mass caused by PMMs and from fluxes due to coastal erosion were calculated using Eq. (15) and Eq. (16), where q_{POC} (tC m^{-1}) represents the POC from the displacement of the peat mass caused by PMMs. J_{POC} (tC m^{-1}

yr^{-1}) represents the POC fluxes due to coastal erosion, l (m) represents the coastline distance, Δt (yr) represents the years of interval for coastal erosion. The POC from the displacement of peat mass caused by PMMs was not measured by fluxes, as PMMs are a sudden disaster. Instead, it was calculated based on the areas that had already collapsed by each date. In general, peat mass movements in boreal peatlands only uses the unit without time such as m^3 or tons to evaluate the magnitudes of these events (Dykes and Warburton, 2007).

$$q_{POC} = M_{PMMs}\, l^{-1} \quad (15)$$

$$J_{POC} = M_{CE}\, l^{-1}\, \Delta t^{-1} \quad (16)$$

The calculated POC shows the standard deviation (SD) of five patterns, including the values from the literature.

4 Results and discussion

4.1 Generation of digital terrain models and characteristics of landslide-affected area

As a result of the machine learning of the landcover classification using NDVI and NDMI, we got the partition line separating vegetation area and bare land area given by Eq. (17). Validation results of the machine learning were as follows: true positive rate, 0.8804; recall, 0.6940; specificity, 0.9950; precision, 0.9885; negative predictive value, 0.8410; and F-score, 0.4077.

$$NDMI = 0.5198 NDVI + 0.7505 \quad (17)$$

Fig. 8 shows the differences in the DEMNAS before and after vegetation removal. The median elevation values of the bare land within 1 km from coastline were used in the vegetation removal from the DEMNAS data. Comparison between ground surface geodetic survey results by Real Time Kinematic-Global Navigation Satellite System (RTK-GNSS) and DEMNAS data after vegetation removal are presented in Fig. 9. The RMSE of the ground elevation obtained from the RTK-GNSS and DEMNAS data after vegetation removal was 0.6951 m. The RMSE was subtracted from the DSM obtained from the UAV aerial photogrammetry to match the DEMNAS elevation. This elevation difference can be caused from the skewness by the elevation decline because of the waterway.

An analysis of the correlation between the area and volume/area of PMMs from 2017 to 2018 in the coastal area of the oil palm plantation is presented in Fig. 10 and Eq. (18), Eq. (19), where V_{PMM} represents the loss of peat volume by PMMs (m^3), and A_{LS} represents the landslide-affected area (m^2).

$$\frac{V_{\mathrm{PMM}}}{A_{\mathrm{LS}}} = 3.0 \times 10^{-5} A_{\mathrm{LS}} + 0.9121 \quad (R^2 = 0.2687) \quad (18)$$

$$f(A_{\mathrm{LS}}) = 3.0 \times 10^{-5} A_{\mathrm{LS}}^2 + 0.9121 A_{\mathrm{LS}} \quad (19)$$

A linear relationship was observed between the landslide area and volume of the peatlands. If the V_{PMM} / A_{LS} is assumed to be the depth of the landslide-affected area, the higher the A_{LS}, the deeper the depth of the collapse. When collapse also occurs, it will be as deep as 1 m. The smallest collapse had an area of 0.11 ha and a volume of 491 m^3. The largest collapse had an area of 3.70 ha and a volume of 85,173 m^3. On average, the landslide-affected areas measured 1.51 ha in area and

22,546 m^3 in volume. The relationship between the volume exported to the ocean by peat mass movements (V_{PMM}) and landslide-affected area (A_{LS}) on Bengkalis Island indicates that the average reduction in ground level ($d_{PMM} = V_{PMM} / A_{LS}$), which ranged from 0.94-1.93 m (mean value = 1.33 m), increased with the area of landslide-affected area (A_{LS}). The ground-level drop was found to be around 0.91 m in small collapses. The depths of peatland degradation varied, but typically in boreal peatlands, blank peat degradation occurred at a depth of 0.6-3 m (Warburton et al., 2004). Koyama et al., 2018 performed geotechnical investigation results in the northwest of Bengkalis Island and revealed a tendency for sedimentary peat to be less than approximately 2 m below groundwater level and the penetration strength to decline. Furthermore, the average difference between the pre-collapse ground elevation and the bottom surface of the peatland cracks was 2.01 m, which indicates a possible correlation between the peatland degradation slide surface and sedimentary peat location.

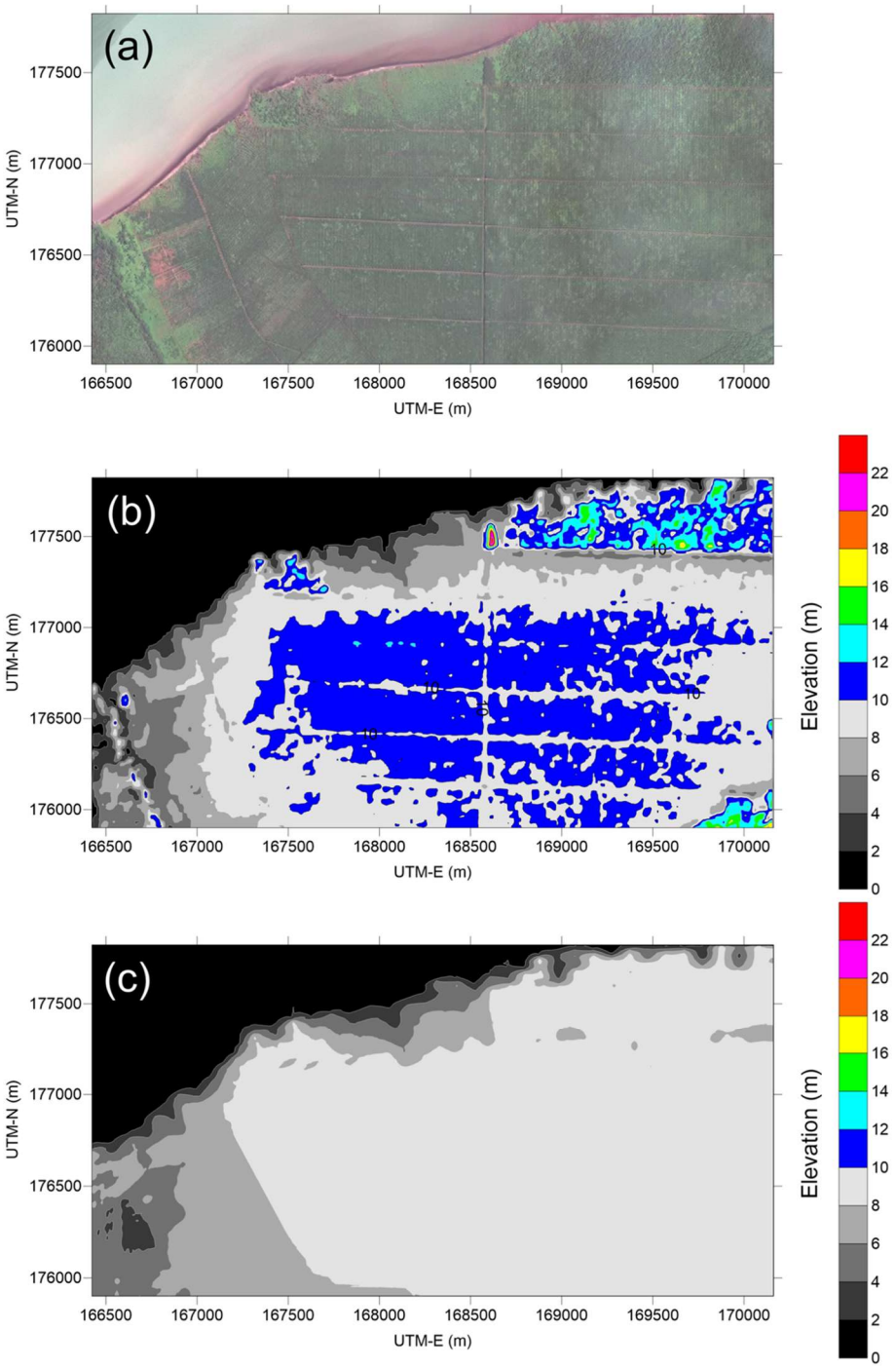

Figure 8: Comparison of (a) SPOT-6 data with (b) original DEMNAS data with (c) DTM removed from vegetation. The elevation of the bare land above 0 m was used to interpolate and generate a DTM with an 8 m resolution by kriging.

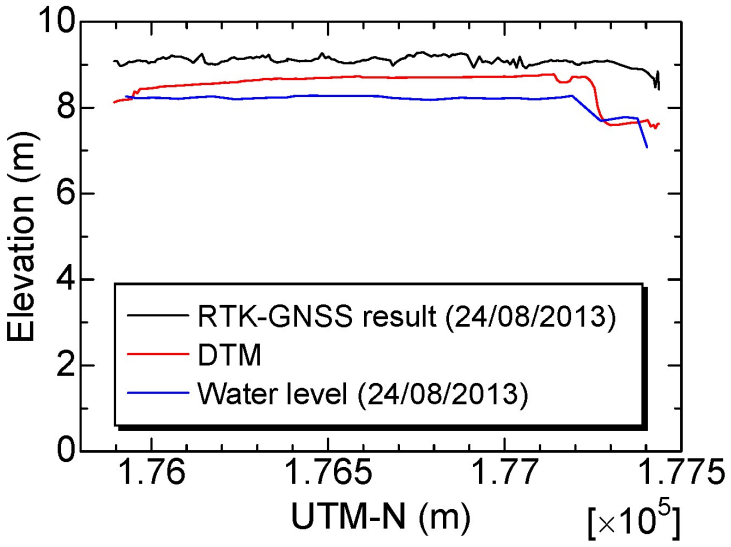

565 **Figure 9: Comparison of the RTK-GNSS land survey with a section created from DEMNAS data. The section where the elevations of DTM has decreased was the section where the collapse was identified in December 2013 after the RTK-GNSS land survey. The RMSE of removing the landslide-affected area was 0.6951 (m).**

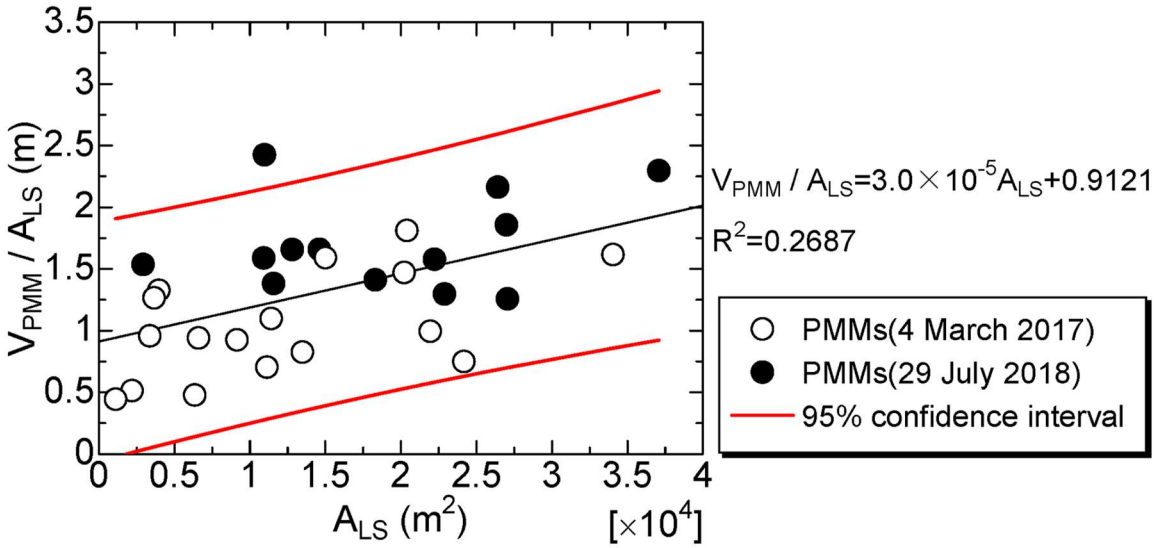

570 **Figure 10: Area-Volume/Area relationship of a peat mass movement event. Where, A_{LS} is landslide-affected area, V_{PMM} is the loss of the peat volume due to a PMM event. There is a linear relationship between A_{LS} and V_{PMM} / A_{LS}; If V_{PMM} / A_{LS} is assumed to be the depth of landslide-affected area, the greater the A_{LS}, the deeper the depth of the collapse. It was found that the ground level drop was around 0.91 m in small collapses.**

4.2 Identification of the timing of peat mass movement events

Fig. 11 shows the temporal changes in elevation along survey section A–A′. Variations in elevation indicate the occurrence of surface tears. In the section corresponding to UTM-N from 177,300 m to 177,400 m, the elevation decreased by an average of 2.01 m between 24 August 2013 and 11 March 2014. UAV-based aerial photogrammetry conducted on 17 December 2014 revealed that a peat collapse had occurred (Fig. 4c (A1)).

Fig. 12 displays an image obtained by SPOT-6 satellite imagery, UAV-based orthomosaic images and calculating the VARI from UAV-based orthomosaic image in which only the exposed peat substrate is delineated. The extent of this PMM was estimated at 8.95 ha in area, with a volume of 321,940 m³, an aperture length of 296 m, and a length of 379 m. The landslide-affected area spans peat swamp forests, oil palm plantations, and shrublands. Furthermore, since 18 September 2013, the coastline has extended seaward, forming a fan-shaped deposit of peaty debris.

Next, the timing of the PMM was determined. In this analysis, the characteristic discontinuity in surface vegetation resulting from the collapse was used to pinpoint its timing. Changes in NDVI and vegetation cover were plotted as a time series to highlight where the vegetation became discontinuous. Fig. 13a illustrates the relationship between vegetation cover and NDVI which exhibits a clear correlation, as expressed by Eq. (20) (with VC representing vegetation cover and $NDVI_{\text{Sentinel-2}}$ representing NDVI of Sentinel-2). Additionally, a strong correlation was observed between the NDVI values from Landsat 8 and Sentinel-2; this relationship is shown in Fig. 13b and expressed by Eq. (21), where x is the $NDVI_{\text{Landsat8}}$ from Landsat 8 and $NDVI_{\text{Sentinel-2}}$ is that from Sentinel-2.

$$VC = 1.5692NDVI_{Sentinel-} - 0.3817 \quad (R^2 = 0.8582) \tag{20}$$

$$NDVI_{Sentinel-} = 1.2578NDVI_{Landsat8} - 0.2349 \quad (R^2 = 0.9571) \tag{21}$$

Fig. 14 presents the time series of vegetation cover for the peat collapse area identified in Fig. 4c (A1). The vegetation cover dropped sharply from 0.87 on 27 December 2013 to 0.21 on 13 February 2014, indicating that the collapse occurred between these dates.

Moreover, along survey section A–A′ in the UTM-N range from 177,000 m to 177,300 m, the elevation decreased by an average of 2.07 m between 20 August 2014 and 10 January 2015 (Fig. 11). UAV-based aerial photogrammetry on 10 January 2015 confirmed that this decrease in elevation was due to a peat (Fig. 4c (A2)). Areas exhibiting fluctuating elevations indicate the presence of peat rafts—blocks of peat displaced by the collapse (Warburton et al., 2004). Fig. 15 shows an image obtained by SPOT-6 satellite imagery, UAV orthomosaic images and calculating the VARI from UAV orthomosaic images, with only the exposed peat substrate delineated. In this case, the PMM was estimated to cover an area of 14.9 ha with a volume of 0.068 km³, an aperture length of 303 m, and a length of 554 m. The PMM also resulted in the formation of a large peaty debris fan, which had an area of 13.7 ha, an aperture length of 583 m, and a length of 268 m; the formation of such an extensive fan underscores the large scale of the collapse.

The time series of vegetation cover at the landslide-affected area (Fig. 14) shows that between 27 October 2014 and 16 February 2015 the vegetation cover decreased rapidly from 0.82 to 0.48, suggesting that the PMM occurred during this

period. Furthermore, Sentinel-1 satellite imagery indicates that approximately 18.4 ha of land area expanded abruptly between 22 December 2014 and 28 December 2014 (Fig. 14), clearly indicating that a large-scale collapse occurred during this interval.

Fig. 16 presents the water level data alongside rainfall data from Selatbaru at the landslide-affected area. During the observation period, the maximum rainfall recorded was 107.9 mm day^{-1} on 23 December and 84.1 mm day^{-1} on 26 December. Following this record rainfall, the water level in the waterway suddenly dropped on 27 December 2014. Although the crest level of the waterway is 9.00 m, the water level was recorded at 9.124 m at 11:10 on 27 December 2014 and then fell sharply to 7.896 m just ten minutes later (Fig. 16). This abrupt decrease suggests that a breach of the weir occurred between 11:10 and 11:20 on 27 December 2014, triggering the PMM. It was also confirmed that the on-site water level logger had shifted by approximately 30 m. The changes in coastal topography indicate that, because of the PMM, peat was exported into the marine environment. At the study site, continuous rainfall exceeding 20 $mm \cdot h^{-1}$ was recorded from 21 December to 26 December, suggesting that the precipitation after 21 December may have triggered the collapse on 27 December.

Boylan et al., 2008 investigated the relationship between the runout distance and failure volume of 44 recorded peat landslides in northern parts of the United Kingdom (particularly the North Pennines) and throughout Ireland (particularly Connacht and Munster). According to this data, the runout distance generally increases with failure volume, although there is considerable variability. Larger failure volumes and consequently longer runout distances tend to occur in raised bogs, which contain deeper and more extensive peat deposits. The long runout of peat landslides can be transported over long distances when they enter rivers and streams and mix with floodwaters. Nout distance can reach up to approximately 7000 m, and the failure volume can reach up to approximately 10,000,000 $m^{3.}$ Specifically, the PMM in Fig. 12 is smaller in scale than the peat landslides in boreal peatlands. However, compared to the boreal peatland landslides in Fig. 15, it has a shorter runout distance but a volume that is 6.8 times larger.

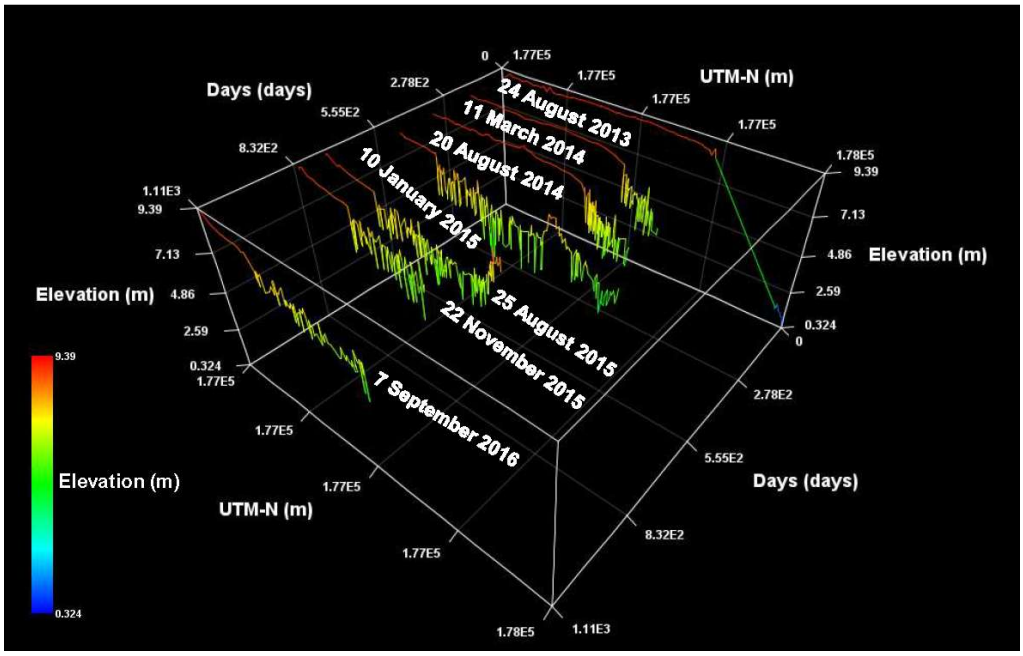

Figure 11: The change in temporal elevation in Section A-A'. The elevation decreased due to PMM from 24 August 2013.

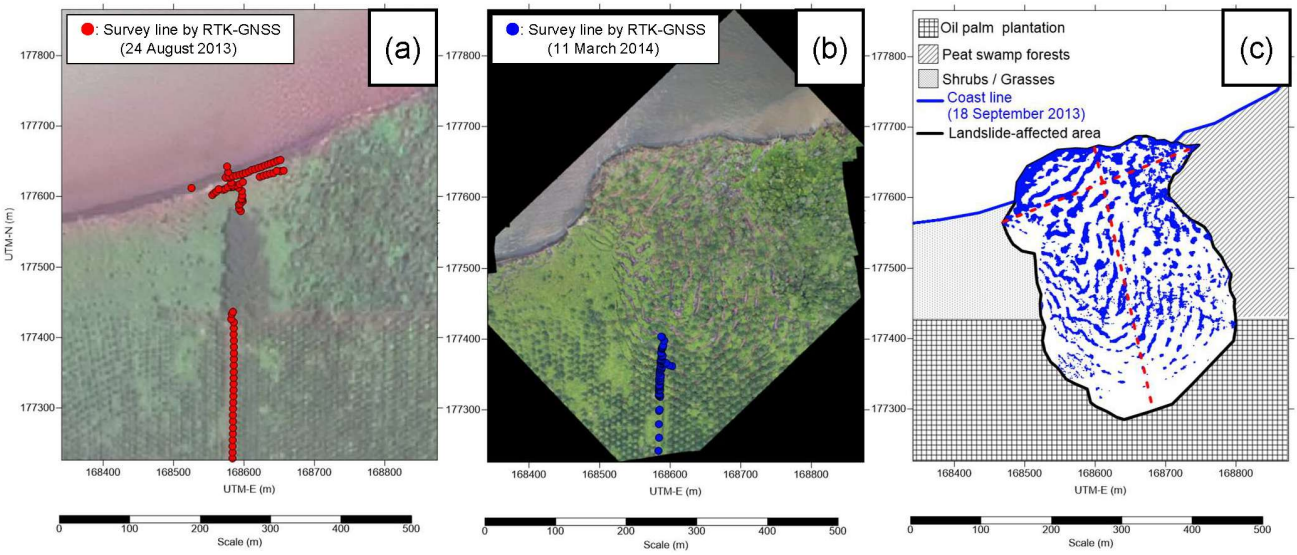

Figure 12: (a) SPOT-6 image (18 September 2013) and (b) UAV-based orthomosaic image (17 December 2014), and (c) anatomy of the landslide-affected area. The scale of the landslide-affected area is as follows: the affected area is 8.95 ha, the volume is 321,940 m³, the length is 379 m, and the aperture length is 296 m. The collapse extended over or into peat swamp forests, oil palm plantations, and shrub areas.

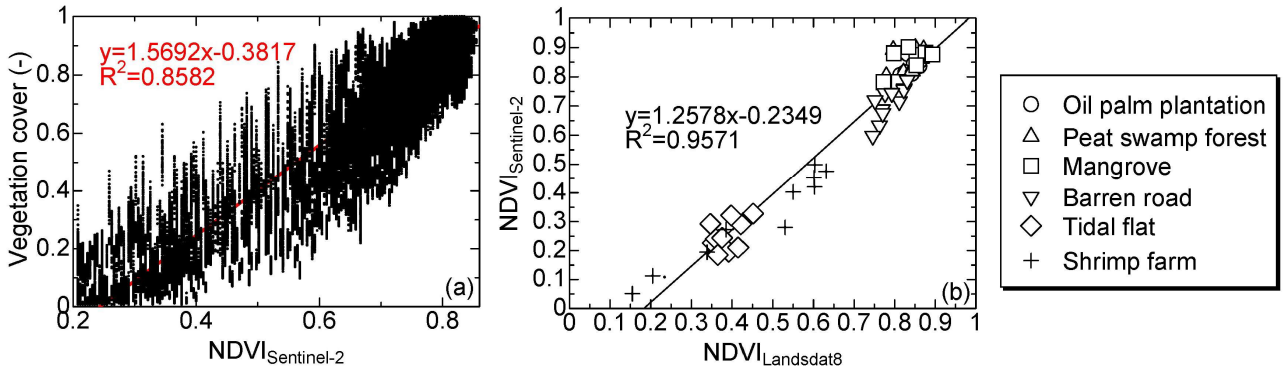

Figure 13: (a): Relationship between Sentinel-2 NDVI and vegetation cover (b): Relationship between Landsat 8 NDVI and Sentinel-2 NDVI, and Both figures show a linear relationship.

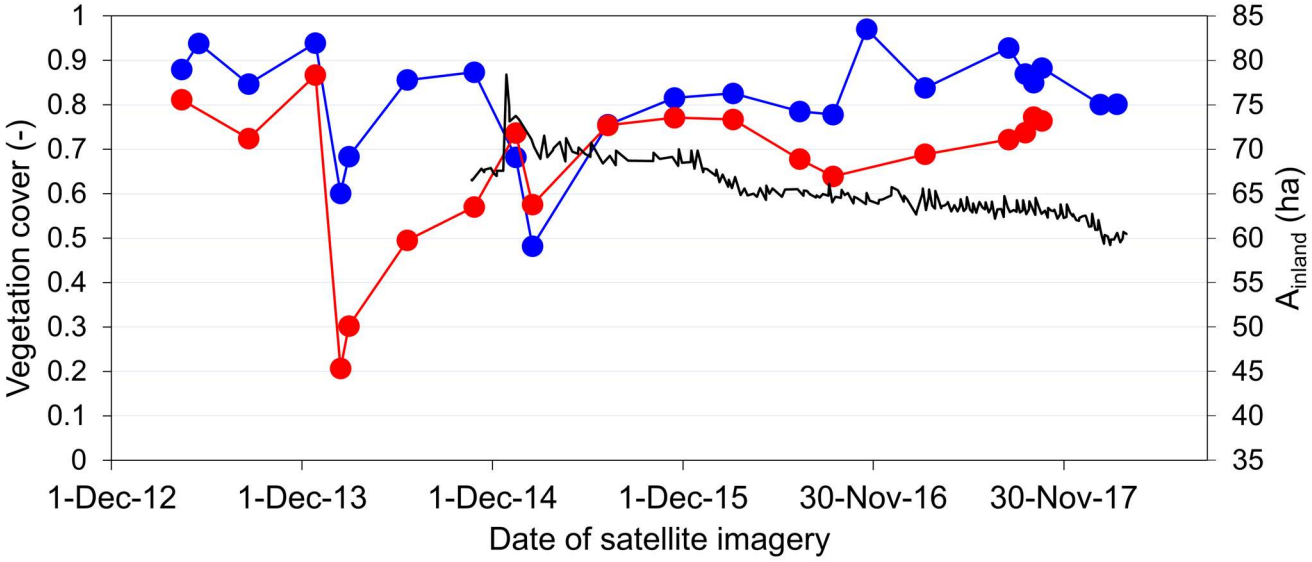

Figure 14: Time series of vegetation cover in landslide-affected areas. Vegetation covers rapidly decreased from 27 December 2013 to 13 February 2014, dropping from 0.87 to 0.21 (A1). Similarly, vegetation covers rapidly decreased from 27 October 2014 to 16 February 2015, declining from 0.87 to 0.48 (A2). The land experienced a sudden extension, increasing by approximately 18.4 ha between December 22 and 28, 2014 (A2).

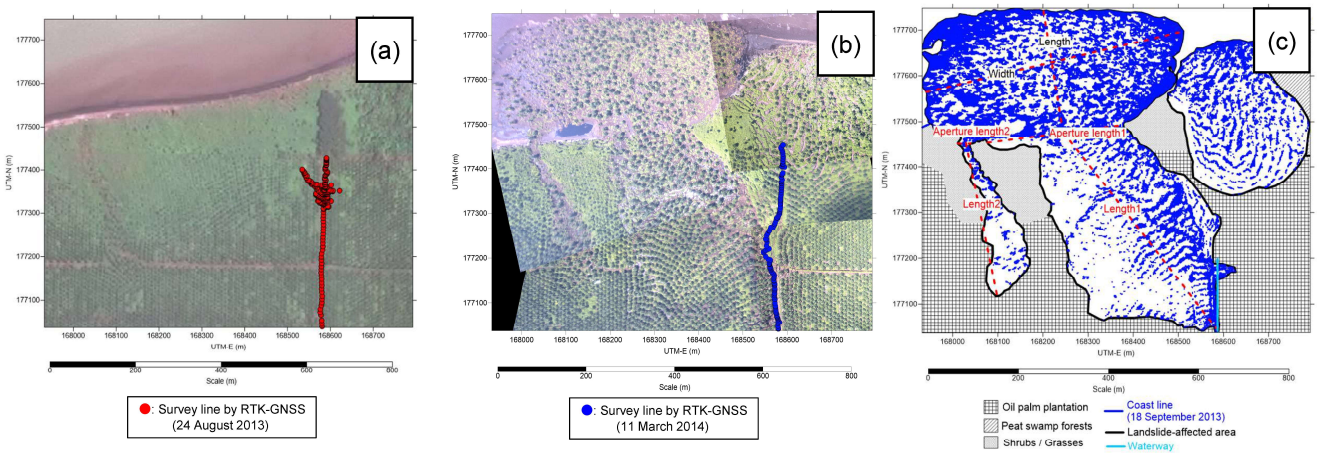

Figure 15: (a) SPOT-6 image (18 September 2013), (b) UAV-based orthomosaic image (10 January 2015), and (c) anatomy of the landslide-affected area. The scale of the landslide-affected area is as follows: the area is 14.9 ha, the volume is 0.068 km³, Length 1 is 554 m with an aperture length of 303 m, and Length 2 is 341 m with an aperture length of 28 m. The scale of the peaty debris fan is as follows: the area is 13.7 ha, the length is 268 m, and the width is 583 m.

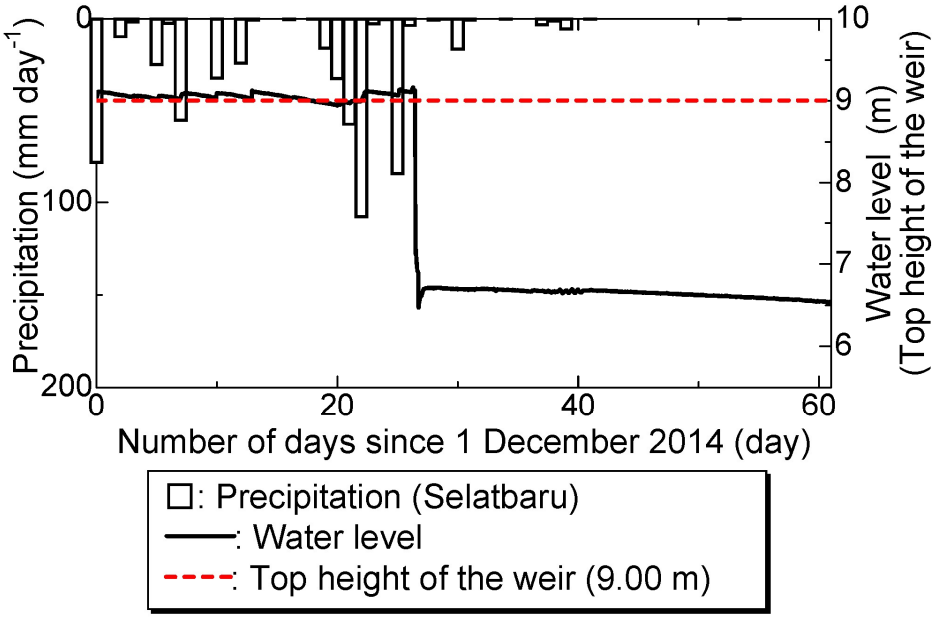

Figure 16: Water level of the water way at P02 and precipitation at Selatbaru station during the peat mass movement event on 27th Dec. 2014. The major precipitations before the event were 107.9 mm day^{-1} (Dec. 23) and 84.1 mm day^{-1} (Dec. 26). Subsequently, the water level of the water way dropped suddenly on Dec. 27, 2014. The top height of the weir was 9.00 m, but the water level was recorded at 9.124 m at 11:10 on December 27, 2014, followed by a sudden drop to 7.896 m just 10 minutes later.

4.3 Estimation of coastal retreat

Based on the long-term changes observed in SAR imagery, along with local meteorological and mooring observations, the actual state of coastal erosion along the northern coast of Bengkalis Island was elucidated using land cover information and meteorological conditions. Fig. 17 shows the cumulative retreat of the coastline by land cover type from 2018 to 2021, as derived from Sentinel-1 data, alongside concurrent meteorological observations. Although coastal erosion has progressed in all land types including mangrove area, oil palm plantations, and peat swamp forests the erosion rate in oil palm plantations is more than twice that observed in mangrove area and peat swamp forests. Moreover, between 2018 and 2021, coastal erosion in oil palm plantations proceeded at an average rate of 3.5 m per 30 days, exceeding the typical average during Indonesia's rainy season, with the highest rate recorded at 24.8 m per 30 days in January 2020. These results suggest that elevated wave heights induced by seasonal winds may accelerate the erosion process.

Fig.18 illustrates the relationship between significant wave height and maximum wind speed, demonstrating that higher wind speeds correspond to greater significant wave heights. Additionally, annual wind roses for Perapat Tunggal and Selatbaru for 2018 and 2021 are presented in Fig.19. In Perapat Tunggal, both years exhibit dominant winds from the west and northwest throughout the year, with westerly winds accounting for 16.39% of the observations and a maximum wind speed of 65 m s^{-1} recorded at 14:30 local time on 30 October 2018. In contrast, in Selatbaru, winds from the east and northeast predominated in both years; in 2018, easterly winds were most frequent at 15.20%, and in 2021 a maximum wind speed of 20.3 m s^{-1} was recorded.

Along the northern coast of Bengkalis Island, the lateral degradation of the mangrove areas has exposed the underlying peat substrate to coastal processes. Under the prevailing tidal and wave conditions, three types of erosion and progressive failure namely, toppling failure, rotational sliding, and cantilever failure have been documented (Basir et al., 2023). Consequently, during seasons characterized by dominant high wind speeds, increased wave heights may further accelerate coastal erosion.

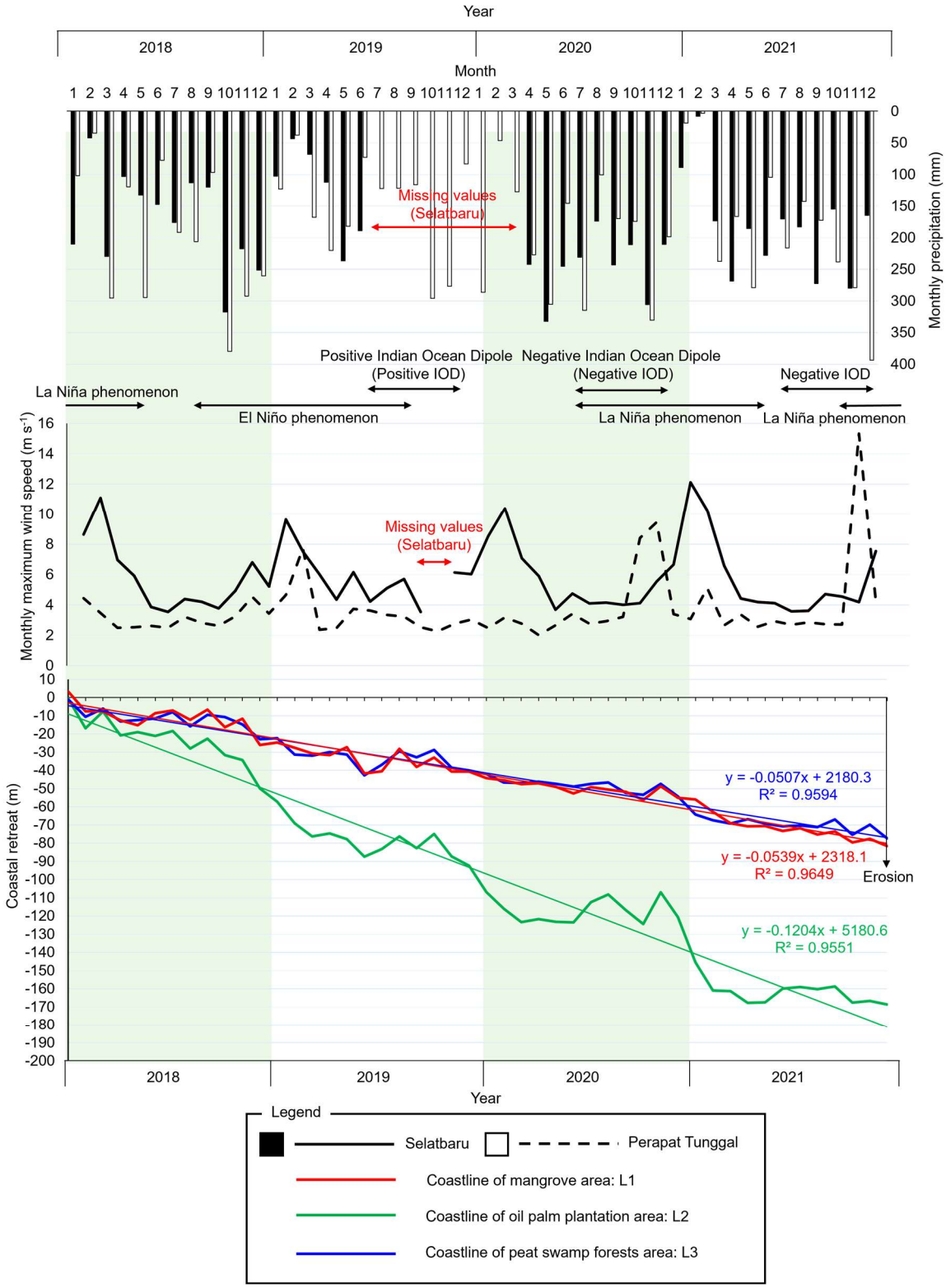
Year
2018
2019
2020
2021
Month
Monthly precipitation (mm)
Missing values (Selatbaru)
Positive Indian Ocean Dipole (Positive IOD)
Negative Indian Ocean Dipole (Negative IOD)
Negative IOD
La Niña phenomenon
El Niño phenomenon
La Niña phenomenon
La Niña phenomenon
Monthly maximum wind speed (m s-1)
Missing values (Selatbaru)
Coastal retreat (m)
y = -0.0507x + 2180.3
R² = 0.9594
y = -0.0539x + 2318.1
R² = 0.9649
Erosion
y = -0.1204x + 5180.6
R² = 0.9551
Year
Legend
Selatbaru
Perapat Tunggal
Coastline of mangrove area: L1
Coastline of oil palm plantation area: L2
Coastline of peat swamp forests area: L3

Figure 17: Cumulative coastline retreat by land cover type from 2018 to 2021, derived from Sentinel-1 data, alongside concurrent meteorological observations. Coastal erosion has progressed across all land types, including mangrove areas, oil palm plantations, and peat swamp forests. However, the erosion rate in oil palm plantations is more than twice that in mangrove areas and peat swamp forests. Erosion is further accelerated by the prevailing monsoon winds during the winter in the northern hemisphere.

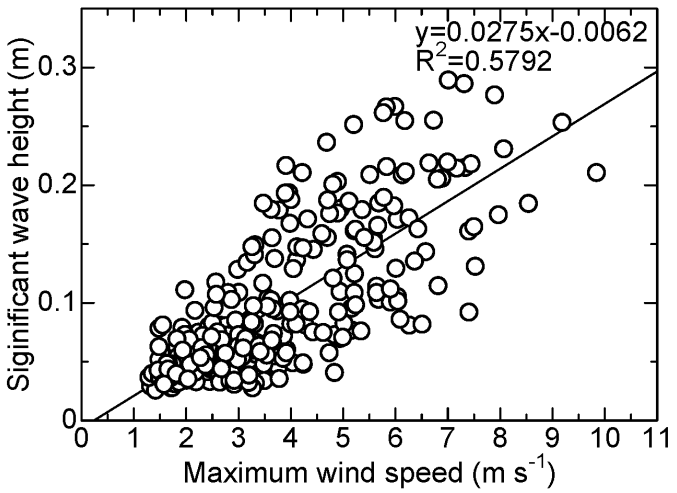

Figure 18: Relationship between maximum wind speed and significant wave height.at the offshore of the Bengkalis Island (St. M).

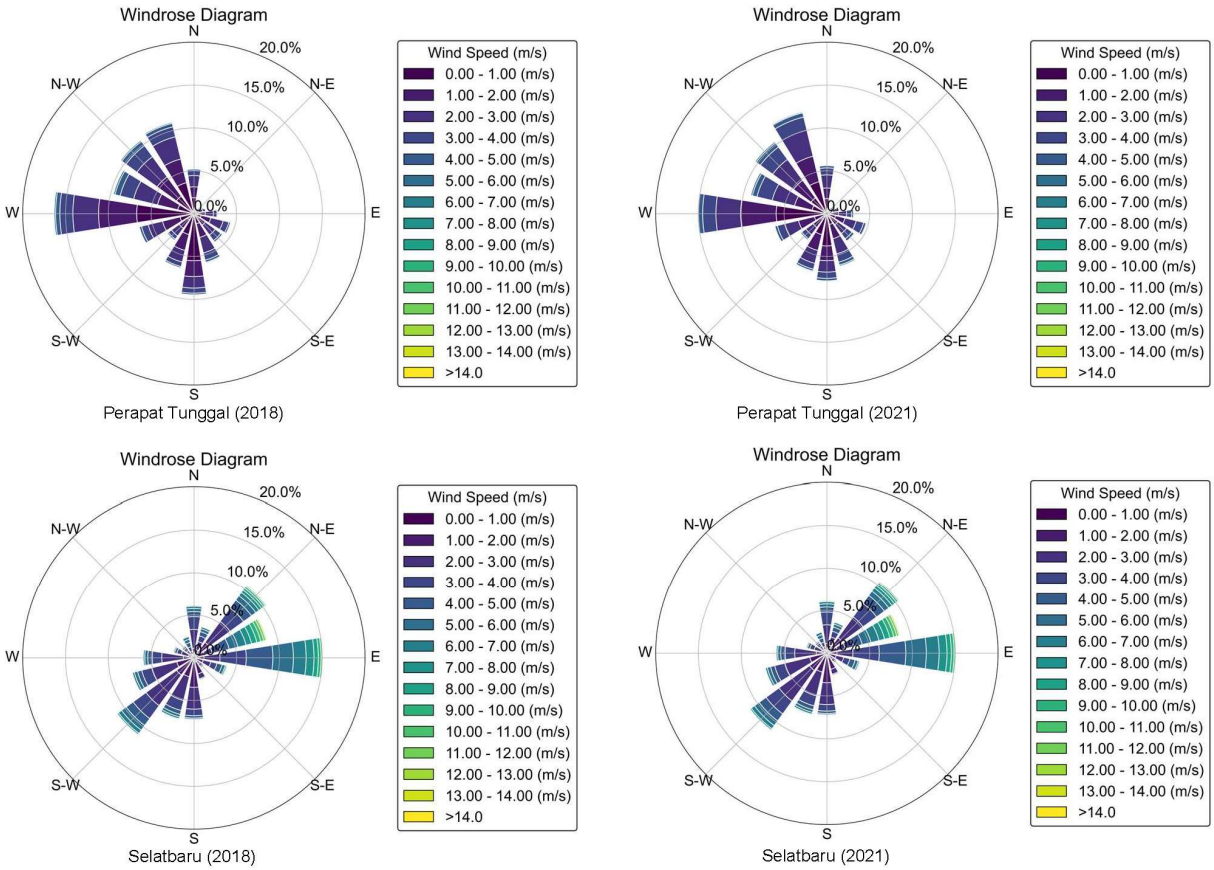

Figure 19: Annual wind rose diagrams for Perapat Tunggal and Selatbaru in 2018 and 2021.

4.4 Lateral degradation process of tropical peatland coasts

In tropical coastal areas, coastal erosion is accompanied by PMMs. A common characteristic of coastal land collapses is the spontaneous release of peat masses from the inland to coastal regions due to concentrated rainfall, which forms a peaty debris fan-shaped terrain. This article presents a one-year interval field observation study reporting the occurrence of a PMM event accompanied by coastal erosion. Fig. 20 shows the annual changes in the area affected by landslides in the northwest area of Bengkalis Island. Following the PMM event, continuous coastal erosion resulted in traces of collapse. The land area initially increased after the PMM event but subsequently decreased during coastal erosion. Fig. 20a shows a high-resolution satellite image (SPOT-6) captured on 18 September 2013, which depicts the state before the PMM event. At the concerned site, the southern part consists of an oil palm plantation and the northern part consists of a peat swamp forest. Although the state of the PMM event after capture is uncertain, given the consistent coastal erosion in this area since 1972, according to Landsat images, coastal erosion could have occurred after the collapse. Fig. 20b shows the area affected by the landslide after the PMM event

photographed by UAV on 17 December 2014. Peat masses migrated from inland to the coast and formed a peaty debris fan. The fan extended offshore beyond the coastline on 18 September 2013. The area of the peaty debris fan formed is 0.80 hectares. Further inland, pull-apart cracks were observed, which could have been caused by the gushing of peat toward the coast. From 18 September 2013, coastal erosion has continued in non-cracked coastal areas. This phenomenon indicates continued coastal erosion even before any coastal PMM event. Fig. 20c shows the conditions captured by the UAV on 10 January 2015. A larger PMM event occurred on the western side of the coastal PMM event, as identified in the previous year. UAV observations resulted in the identification of a larger, peaty debris fan-shaped structure that was not confirmed on 17 December 2014. The structure of the peaty debris fan-shaped land formed by the movement of peat masses was observed to have changed, although no significant changes were observed in the PMM event on 17 December 2014. Fig. 20d shows the UAV results from 5 March 2016. The peaty debris fan-shaped land caused by the large-scale PMM event in the west on 10 January 2015, had disappeared. The peaty debris fan-shaped land formed due to the PMM event on 17 December 2014, notably disappeared on 10 January 2015. Between 10 January 2015 and 5 March 2016, the peaty debris fan was gradually eroded from the east by waves (Fig 20d). Fig. 20e shows the UAV results for 4 March 2017. The peaty debris fan-shaped land that jutted out from the coastline on 18 September 2013, formed due to the PMM event on 17 December 2014, had completely disappeared by 4 March 2017, and the coastline retreated from its original position on 18 September 2013. Fig. 20f shows the UAV results from 29 July 2018. The coastline has receded considerably since September 18, 2013, due to progressive coastal erosion. From 18 September 2013 to 29 July 2018, the coastline receded by approximately 90 m, averaging an annual retreat of approximately 18 m. As shown in this chapter, when a PMM event occurs in the coastal zone, a peaty debris fan is formed, leaving a collapse scar in the hinterland. The coastal erosion then proceeds until peat cliffs are formed.

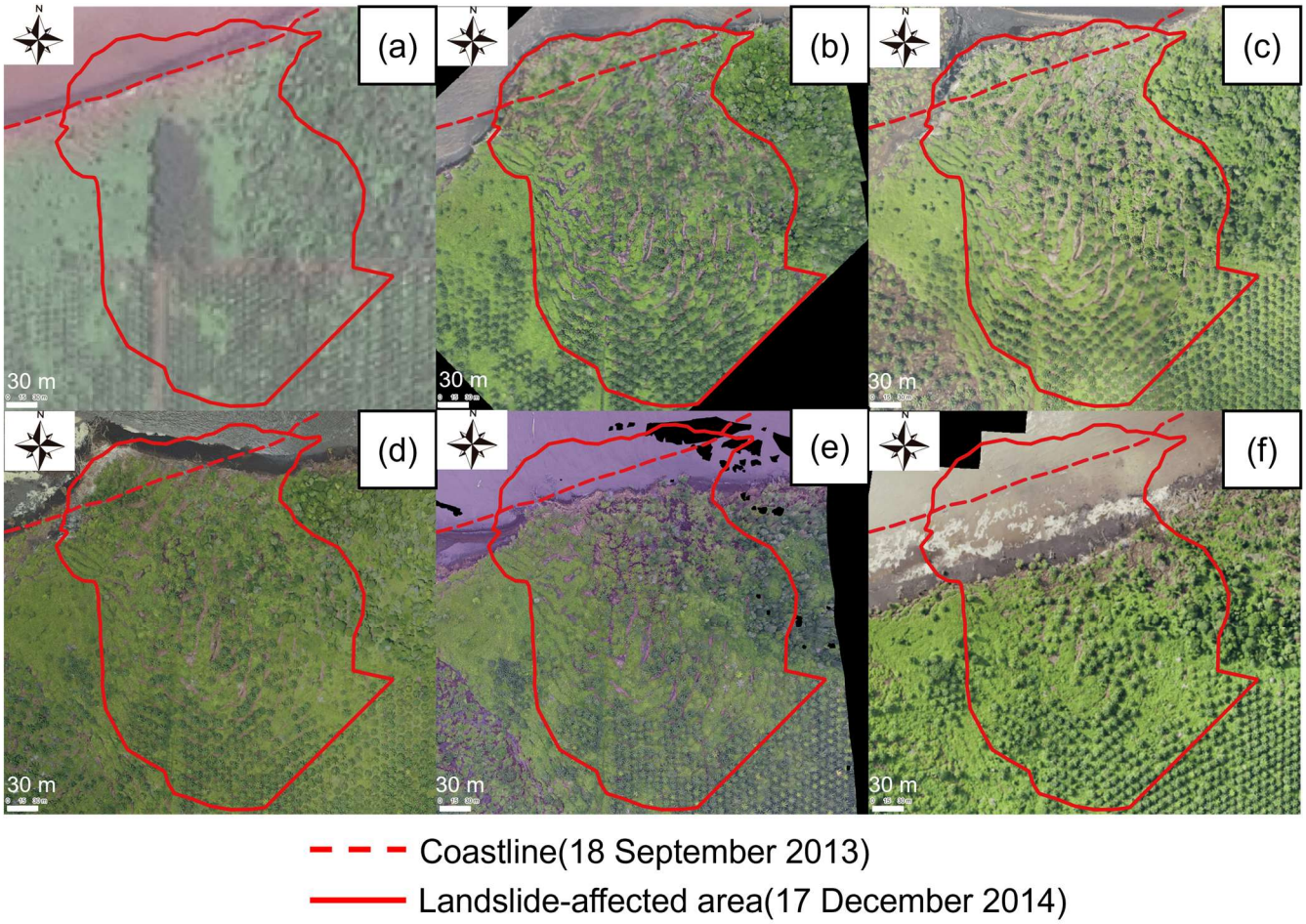

Figure 20: Annual changes at the landslide-affected area in the northwestern part of Bengkalis Island. (a) Initial status of the focus area with a peat cliff coastline (SPOT-6, 18 September 2013). (b) The immediate aftermath of a peat mass movement; a peaty debris fan was confirmed outside the initial coastline, with many tears observed on the ground surface of the hinterland (UAV-based orthomosaic, 17 Dec. 2014). (c) A larger peat mass movement occurred in the western area, creating a second peat fan, while the first peat fan remained (UAV-based orthomosaic, 10 Jan. 2015). (d) The second peaty debris fan in the west area completely disappeared, while the first peaty debris fan remained (UAV-based orthomosaic, 5 Mar. 2016). (e) Gradually, the first peaty debris fan eroded and decreased in area (UAV-based orthomosaic, 4 Mar. 2017). (f) The first peaty debris fan disappeared, and the coastline receded approximately 90 m from the initial status on average, returning to a peat cliff (UAV-based orthomosaic, 29 Jul. 2018).

4.5 Analysis of soil sampling results: distribution of dry density, carbon concentration, and moisture content

Fig. 21 shows the vertical distributions of dry density, carbon concentration, and moisture content. Under the groundwater level, a high moisture content, low dry density, and low carbon concentration were observed. High values of dry density and carbon concentration may have been observed on the surface of groundwater due to oxidative decomposition.

The accumulated organic carbon content was calculated vertically downward from the surface. The accumulated organic carbon content derived from the field survey results and literature values (Wahyunto et al., 2003; Dariah et al., 2012; Warren et al., 2012; Rudiyanto et al., 2018) is shown in Fig. 22. The accumulated organic carbon content was approximated by Eq. (22), using peat obtained from the field survey. where m_c (z) represents the accumulated carbon content (t m^{-2}), and z represents the depth of the peat layer from the ground surface (m).

$$m_c(z) = 0.0982z^{0.679} \quad (R^2 = 0.9636) \tag{22}$$

The results of peat sampling during the field survey could be approximated by the power approximation curve. The higher cumulative carbon content to a depth of 2 m is due to the groundwater table being present at a depth of 2 m, the environment being conducive to oxidative decomposition at the surface, and consolidation results in a higher bulk density. The outflow of particulate organic carbon into the sea due to coastal erosion and peatland degradation was estimated using the power approximation curve relationship described in this section.

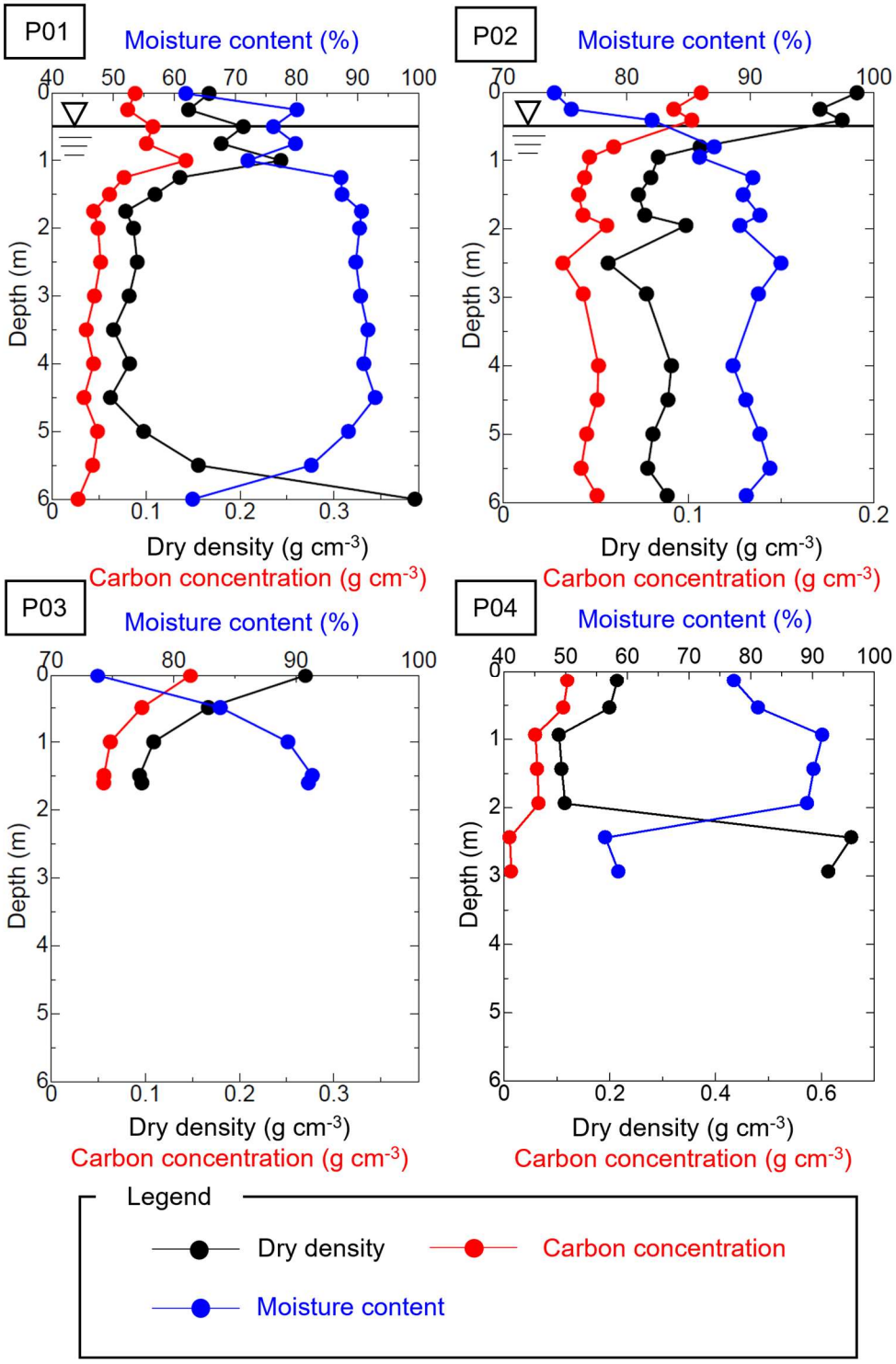

Figure 21: Vertical distribution of dry density of peat, carbon concentration, and moisture content by peat core analysis.

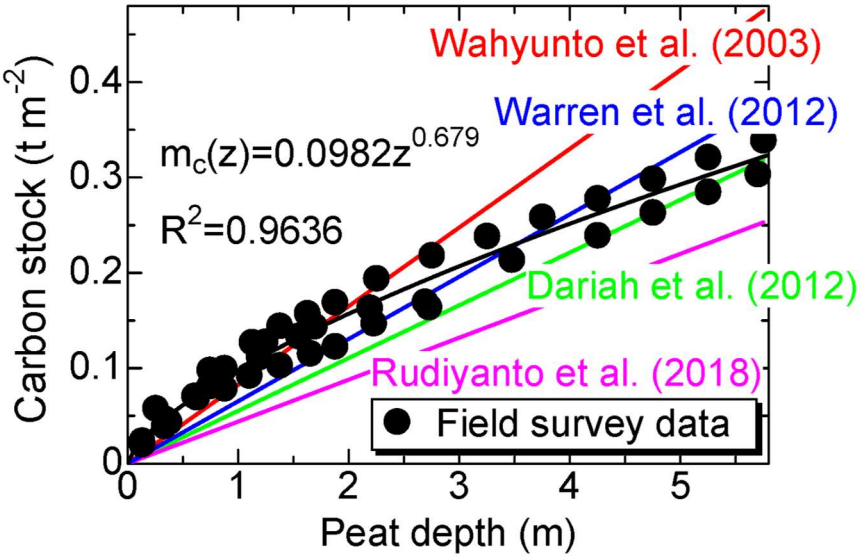

Figure 22: Cumulative carbon content relative to depth. Literature values sourced from Wahyunto et al., 2003; Dariah et al., 2012; Warren et al., 2012 and Rudiyanto et al., 2018. The literature values from Wahyunto et al., 2003 were calculated using average values for the bulk density and carbon content of Hemic peat. Literature values from Dariah et al., 2012 were calculated using a function to estimate carbon stocks according to the depth of the peat layer. The literature values from Warren et al., 2012 were calculated using a function to estimate carbon stocks from average bulk density. Literature values from Rudiyanto et al., 2018 estimated carbon stocks from average carbon content and bulk density.

4.6 Estimation of POC export to the ocean from lateral degradations

We estimated the amount of POC exported to the ocean due to coastal erosion and PMMs. Fig. 23 shows the annual changes in coastal erosion and landslide-affected areas. The estimated amounts of POC flux to the ocean are shown in Fig. 24 and Table 5. The average flux of POCs to the ocean due to coastal erosion along the research area of Bengkalis Island was estimated to be in the range of 2.06 to 7.60 tC m^{-1} yr^{-1}. The average POC from the displacement of the peat mass caused by PMMs along the study area of Bengkalis Island was estimated to be in the range of 1.43 to 5.41 tC m^{-1}, with an average increase of 2.23 tC m^{-1} from 2010 to 2018. In addition to the carbon mass continuously discharged into the ocean due to ongoing coastal erosion, an additional carbon mass is released into the ocean because of sudden PMMs. The POC fluxes from the coastal erosion and the PMMs were calculated for the catchment area (641 ha) of the target coastline (3,152 m) and found that the coastal erosion was 1.01-3.74 kt km^{-2} yr^{-1}, and the PMMs were 0.70-2.66 kt km^{-2}.

Carbon dioxide emissions from drained or logged peatlands can reach 499 g m^{-2} yr^{-1} (Hirano et al., 2014). To put this carbon footprint in perspective, on Bengkalis Island, POC loss from erosion of one metre of shoreline is equivalent to the annual carbon dioxide emissions from 0.41-1.52 ha of drained or cut peatland. And the POC from the displacement of the peat

mass caused by PMMs on Bengkalis Island in our study is equivalent to the carbon emissions produced over a year of 0.29-1.08 ha of drained or logged peatlands, measured as carbon dioxide per metre of coastline. On a peatland coast with an average length of 3,152 m, the amount of POC exported to the ocean due to PMMs were estimated to range from 4.45 ktC to 17.1 ktC, while the POC exported due to coastal erosion was estimated to range from 6.35 ktC yr^{-1} to 23.9 ktC yr^{-1}.

The export of POC from terrestrial to marine environments is primarily driven by riverine transport. A study investigating the relationship between climate, biota, and geomorphological patterns in major river basins worldwide and their impact on organic carbon fluxes predicted that approximately 0.38 GtC of organic carbon are exported to the ocean annually. Of this, about 0.21 GtC are in dissolved form, while approximately 0.17 GtC are in particulate form (Ludwig et al., 1996). Notably, organic carbon export from tropical humid regions accounts for approximately 45% of the total, with most of the dissolved organic carbon entering the Atlantic Ocean and most particulate organic carbon being transported to the Indian and Pacific Oceans (Ludwig et al., 1996). According to Ludwig et al., 1996, the total area of tropical humid regions is 23,633,000 km^2 and the POC discharge to the oceans was estimated to be 81.09 TgC yr^{-1}. Therefore this corresponds to be a POC flux of 3.43 tC km^{-2} yr^{-1}. Comparing to this case, POC flux due to the coastal erosion in the watershed in studied region of 641 ha (Fig. 4) was 295 to 1,089 times greater than the value.

When terrestrial organic matter (TOM) particulate discharges into the ocean, much of it is likely to settle in seawater and accumulate in coastal seabed sediments for decades to centuries. In contrast, dissolved TOM undergoes oxic biodegradation or photolytic decomposition when it rinses oxygen-rich surface waters (Mopper et al., 1991). The annual precipitation in the study area was 2,013 mm (from 1 January to 31December 2018). Assuming an estimated evapotranspiration rate of 4 mm day^{-1} in tropical peatlands, the annual discharge from groundwater and rivers is calculated to be 553 mm. Given a riverine DOC concentration of 62 mg L^{-1}, the estimated annual DOC export is approximately 34 tC km^{-2} (Yamamoto et al., 2020). And approximately 1% of DOC leaches from POC and rinses into the ocean due to PMM or coastal erosion (Yamamoto et al., 2020). Leached DOC can be released as carbon dioxide through oxidative or photolytic decomposition. The carbon load flow in the study area, as determined in this study, is shown in Fig. 25. It is necessary to investigate the fate of deep peat when it is exposed to the atmosphere due to PMMs and erosion or transported into the ocean, including whether it remains suspended at the surface or accumulates on the seafloor. This lateral carbon export along the tropical peatland coast indicates a new route of carbon export to the ocean in addition to the common riverine export of POC to the ocean.

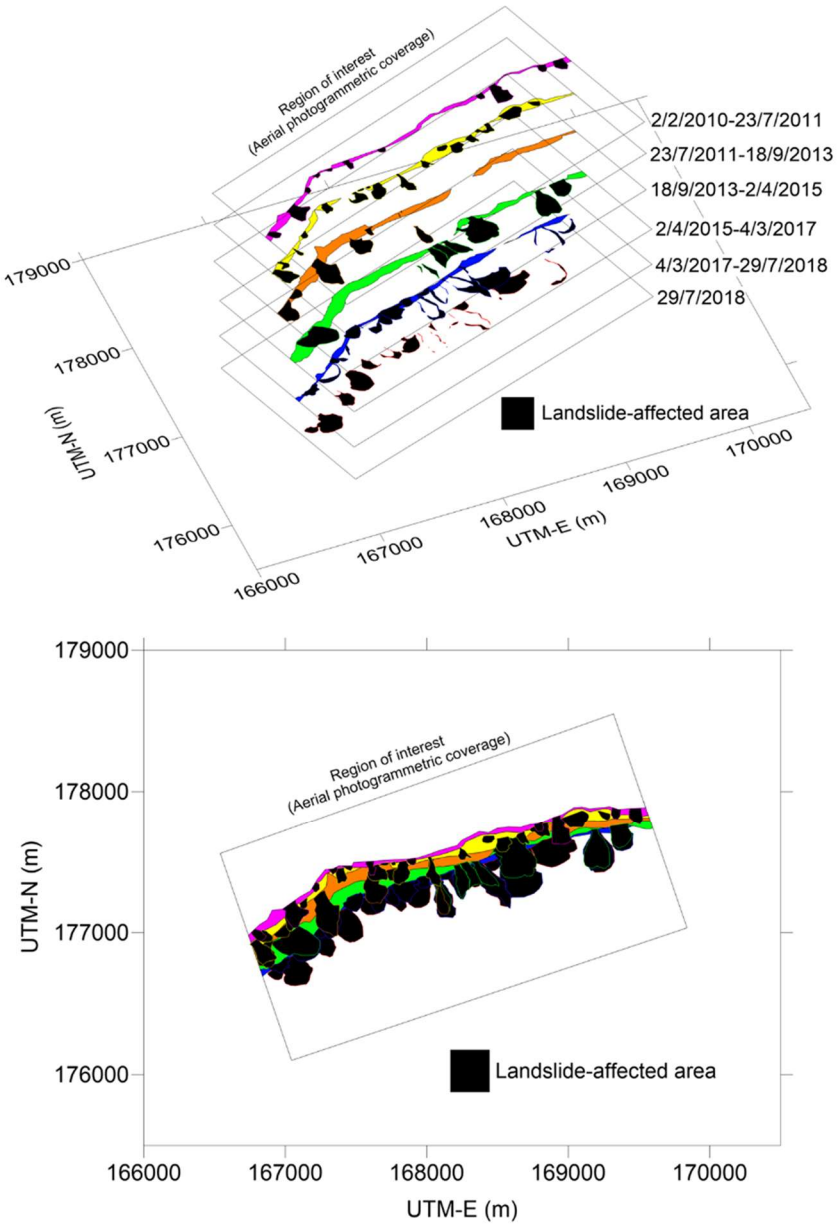

Figure 23: History of coastal erosion and landslide-affected area within the region of interest (68 ha). This figure shows that the coastal erosion and peat mass movements occurred by turn and the landslide-affected area had been expanding towards the hinterland.

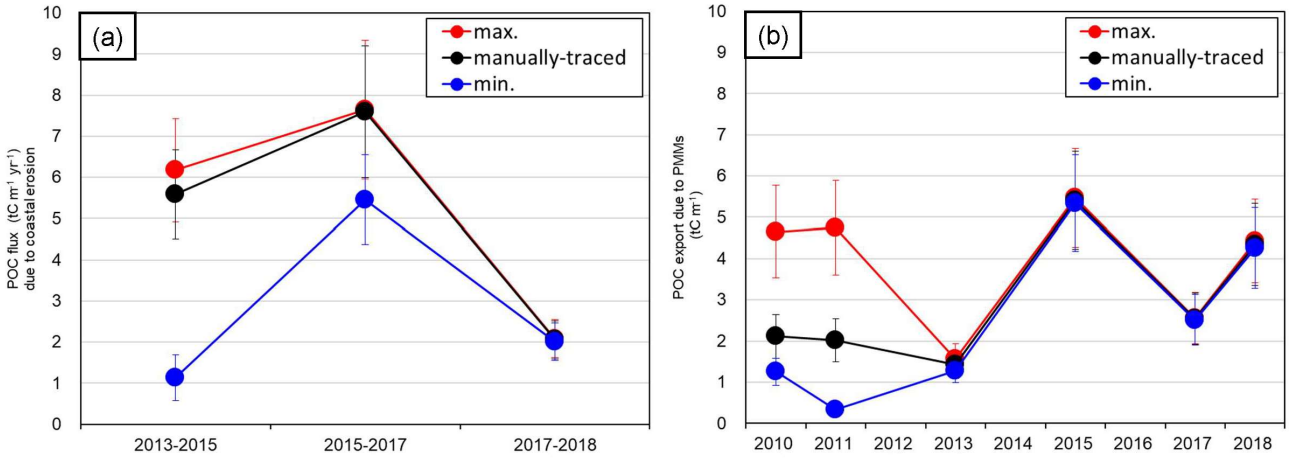

Figure 24: Time series of (a) estimated POC fluxes due to coastal erosion and (b) estimated POC export due to displacement of peat mass caused by PMMs for observation moment. The average POC flux of POC to the ocean was estimated to be 2.06 to 7.60 tC m^{-1} yr^{-1} by coastal erosion and 1.43 to 5.41 tC m^{-1} from PMMs. The error bars indicate the standard deviation (SD).

Table 5: The landslide-affected area and the estimated volume of the eroded peat by the events of coastal erosion and peat mass movements in each period. Changes in time in the estimated amount of POC from peat mass displacement caused by PMMs and from flows due to coastal erosion. SD indicates the standard deviation of the POC flux calculated using the results of five patterns of cumulative carbon content calculations, including values from the literature. Where period (a) is 2/2/2010 to 23/7/2011, period (b) is 23/7/2011 to 18/9/2013, period (c) is 18/9/2013 to 2/4/2015, period (d) is 2/4/2015 to 4/3/2017 and period (e) is 4/3/2017 to 29/7/2018.

Coastal erosion											
Period	Term	Coastline	Area			Volume			POC flux		
			min.	manually-traced	max.	min.	manually-traced	max.	min.	manually-traced	max.
										Average±SD (n=5)	
	days	m		ha			Mm^3			tC m^{-1} yr^{-1}	
(a)2010-2011	536	3,096	1.8	9.7	20.0		-		-	-	-
(b)2011-2013	788	3,313	8.2	13.0	18.6		-		-	-	-
(c)2013-2015	561	3,120	16.8	17.0	18.8	0.24	0.43	0.53	1.13±0.56	5.59±1.08	6.17±1.27
(d)2015-2017	702	3,162	18.4	18.5	18.8	0.64	0.75	0.80	5.46±1.09	7.60±1.60	7.65±1.69
(e)2017-2018	512	3,140	9.6	9.8	9.9	0.130	0.136	0.138	2.02±0.45	2.06±0.46	2.09±0.47
Total	3099		54.8	68.0	86.1	1.01	1.32	1.47			
PMMs											
Date		Coastline	Area			Volume			POC exported rate per unit length		
			min.	manually-traced	max.	min.	manually-traced	max.	min.	manually-traced	max.
										Average±SD (n=5)	
		m		ha			Mm^3			tC m^{-1}	
2/2/2010		3,096	4.8	7.4	14.7	0.06	0.10	0.22	1.25±0.33	2.11±0.53	4.65±1.12
23/7/2011		3,313	3.9	11.8	24.1	0.02	0.14	0.34	0.33±0.13	2.02±0.52	4.74±1.15
18/9/2013		3,120	7.8	8.8	9.8	0.14	0.15	0.16	1.28±0.29	1.43±0.33	1.57±0.36
2/4/2015		3,162	21.0	21.3	21.6	0.395	0.400	0.404	5.34±1.17	5.41±1.18	5.47±1.20
4/3/2017		3,140	16.0	16.2	16.3	0.228	0.230	0.232	2.51±0.61	2.54±0.62	2.56±0.62
29/7/2018		3,085	16.5	16.9	17.3	0.275	0.280	0.285	4.26±0.98	4.34±1.00	4.42±1.02
Total			70.0	82.4	103.8	1.12	1.30	1.64			

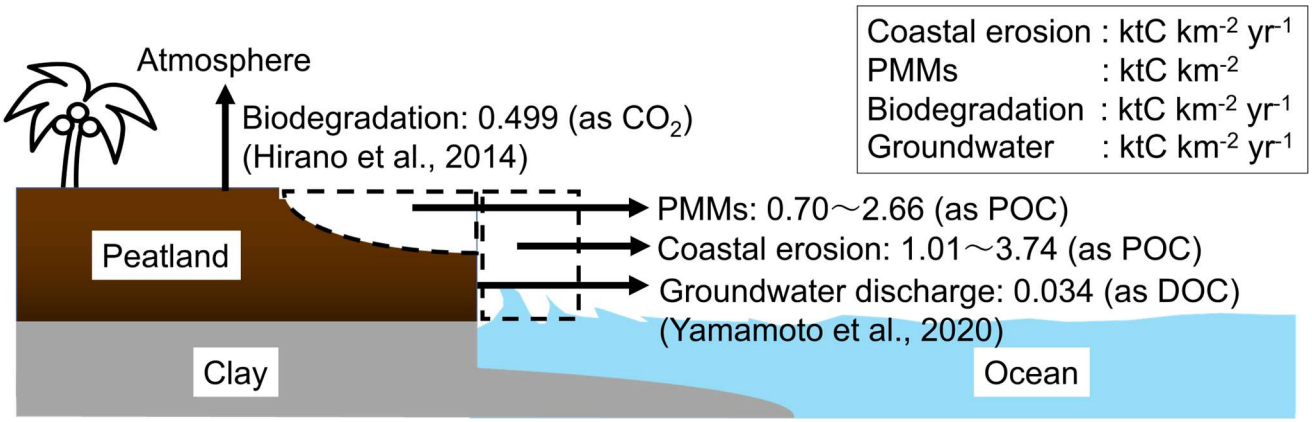

Figure 25: Estimated carbon flux of the watershed in the Bengkalis Island. Biodegradation was referred to Hirano et al., 2014. Groundwater discharge was referred to Yamamoto et al., 2020.

5 Conclusions

In this study, we have identified the conditions under which a chain of coastal erosion and peat mass movement events (PMMs) occur on tropical peatland islands with peat-formed coasts, and we have estimated the export of POCs to the ocean resulting from these processes. In coastal areas of tropical peatlands, coastal erosion promoted peat mass movements and vice versa. This chain of events of coastal erosion and peat mass movements proceeds as follows; When peat mass movement events first occur on a coastal peatland, peat is exported from the coast into the ocean, forming a peaty debris fan. Subsequent erosion causes the peaty debris fan to disappear, leaving the peat cliffs and the area affected by landslides. Long-term progression of coastal erosions has affected carbon export from the peatland. The rate of coastal erosion of oil palm plantations exceeded those of mangrove or peat swamp forests by more than double. The relationship between significant wave height and maximum wind speed indicates that stronger winds correspond to higher wave heights, emphasising the role of wind-induced wave activity in coastal processes. These findings suggest that elevated wave heights, driven by seasonal winds, may contribute significantly to the acceleration of coastal erosion. The POC fluxes due to coastal erosion are estimated to average between 2.06 and 7.60 tC m^{-1} yr^{-1}. PMMs resulted in substantial peat loss and coastal geomorphic changes. The export of peat into the marine environment underscores the significant impact of these collapses on carbon fluxes and coastal dynamics. Heavy precipitation played a crucial role in the triggering of PMM. In the case of December 2014, a weir breach event likely initiated the collapse of the lower reach of the peatland. The POC of the displacement of the peat mass caused by PMMs is estimated to average between 1.43 and 5.41 tC m^{-1}. The carbon export rate in the study watershed (641 ha) due to coastal erosion contributed to an annual carbon export of 1.01-3.74 ktC km^{-2} yr^{-1}, which is 2.0-7.5 times higher than the carbon emissions from peat biodegradation. While the carbon export rate through PMMs contributed to surplus carbon export of 0.70 - 2.66 ktC km^{-2}. On a peatland coast with an average length of 3,152 m, the amount of POC exported to the ocean due to PMMs

was estimated to range from 4.45 to 17.1 ktC, while the POC exported due to coastal erosion was estimated to range from 6.35 to 23.9 ktC yr^{-1}. Compared to the typical POC flux from tropical humid regions via riverine transport, these lateral carbon fluxes in this watershed (641ha) correspond to approximately 295 to 1,089 times greater. Consequently, these lateral carbon exports on tropical peatland coasts represent a new route for carbon export to the ocean, in addition to POC discharges from rivers, in general. However, the fate of exported peat to the ocean needs to be clarified. It is still unclear whether the fate of deep layer of the peat is exposed to the atmosphere due to PMMs, erosion, and transport to the ocean, including whether it remains suspended at the surface or accumulates on the seafloor.

Appendix A: Comparison of optical satellite images and UAV-based orthomosaic and estimation methodology of the volume of the land slide-induced exported peat to the ocean

In this study, optical satellite imagery and UAV-based orthomosaic were used to identify landslide-affected areas and coastlines. A comparison of Landsat8 imagery, which has a resolution equivalent to Landsat5, the lowest resolution of the optical satellites used, and UAV-based orthomosaic Landslide-affected areas at the same location is shown (Figs. A1a, A1b, A1c, A1d and A1e; described in Sect. 3.2.4 and Sect. 3.2.6). Errors due to tracing were considered to vary depending on the resolution of the imagery, such as low-resolution satellite imagery, high-resolution satellite imagery and UAV-based orthomosaic, as the landslide-affected area and coastline cannot be identified unless the zoom is adjusted so that a wide area is visible, depending on the resolution of the imagery (Figs. A1a, A1b, A1c, A1d and A1e; described in Sect. 3.2.4 and Sect. 3.2.6). The process in GIS software of estimated the volume of peat exported to the ocean is shown (Figs. A1e, A1f, A1g, A1h, and A1i; described in Sect. 3.2.3).

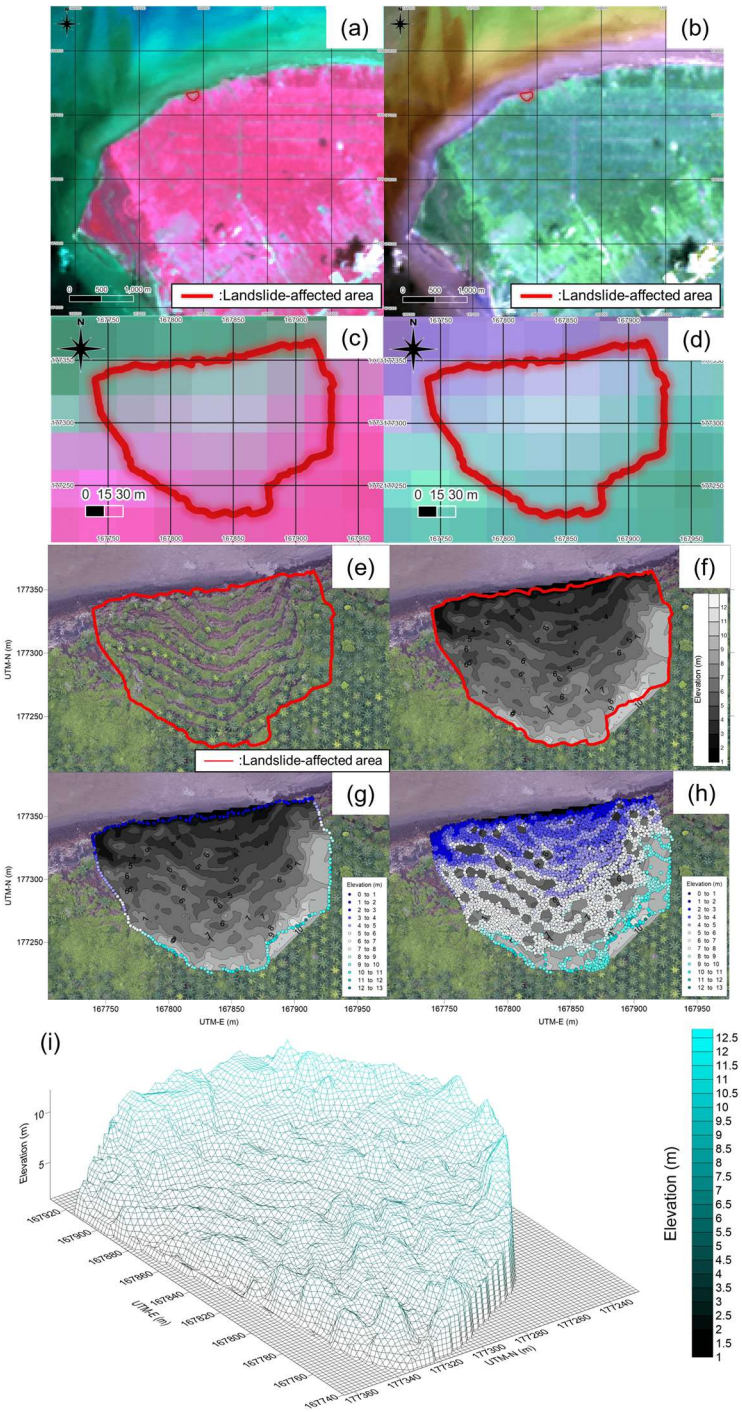

865 **Figure A1: Comparison of optical satellite images and UAV-based orthomosaic and the process in GIS software of estimating the volume of peat exported to the ocean. (a) Landslide-affected-area identified by wide-area visibility and UAV- based orthomosaic (4 March 2017) in Landsat 8 false colour image (9 March 2017). (b) Landslide-affected-area identified by wide-area visibility and UAV-**

based orthomosaic (4 March 2017) in Landsat 8 true colour image (9 March 2017). (c) Landslide-affected-area identified by zoomed-area visibility and UAV- based orthomosaic (4 March 2017) in Landsat 8 false colour image (9 March 2017). (d) Landslide-affected-area identified by zoomed-area visibility and UAV- based orthomosaic (4 March 2017) in Landsat 8 true colour image (9 March 2017). (e) Landslide-affected-area identified by UAV- based orthomosaic (4 March 2017). (f) DEM was post-collapse DEM, which were generated by sampling elevation data in the landslide-affected areas of vegetation removed DSM. (g) Elevation points at the edge of the DSM of the landslide affected area extracted to recreate the initial land surface. (h) Elevation points (4,516 points) inside the DSM of the landslide-affected area extracted to recreate the DEM after collapse. (i) Shape of the collapse site with the vegetation removed.

Appendix B: Error evaluation method for traced coastal erosion areas and landslide-affected areas in GIS software

This study considered traced errors in coastal erosion areas and landslide-affected areas, which were calculated by manual tracing in GIS software. The concept of an error evaluation method for traced coastal erosion areas and landslide-affected areas on GIS software is presented in Fig. B. When considered at the scale of one pixel in the image, it was assumed that the manually traced lines would have trace errors within one pixel. Therefore, the traced error will depend on the resolution. Here, for the case where Google Earth was used, it was assumed that a tracing error equivalent to that of Landsat5 would occur, as the resolution was not opened. For cases where low-resolution images are used, the tracing errors are greater because the landslide-affected area and the coastline cannot be identified without scaling the scale (Figs. A1a, A1b, A1c, A1d and A1e). Errors in tracing planes also affect the calculation of volumes. Traced errors were also reflected in volume calculations.

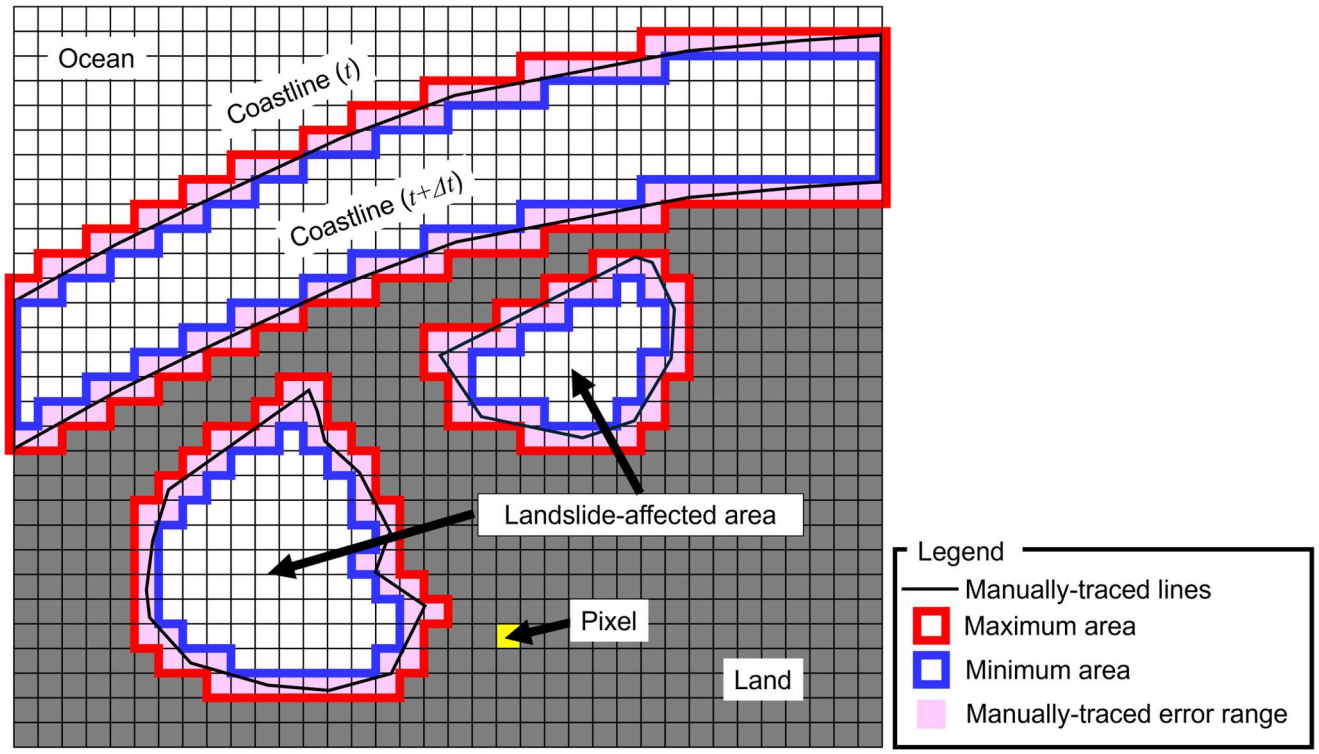

Figure B: Concept of the error evaluation method for traced coastal erosion areas and landslide-affected areas in the GIS software. Manual tracing errors tend to be resolution dependent.

890

Appendix C: Evaluation of resolution-induced errors using Landsat 8 and Sentinel-2 imagery

We evaluated the errors caused by differences in resolution using satellite images from Landsat 8 and Sentinel-2 acquired at the same time (n=7). To achieve this, we conducted 20 tracings per time for comparison. Using Landsat 8 with a 30 m resolution and Sentinel-2 with a 10 m resolution, landslide-affected areas captured at the same time were manually traced, and the error
895 was evaluated (Fig. C). Larger collapses exhibited greater tracing errors, with an overall RMSE of 0.608. ha the results also indicate that tracing variability is greater with Landsat 8, which has a lower resolution.

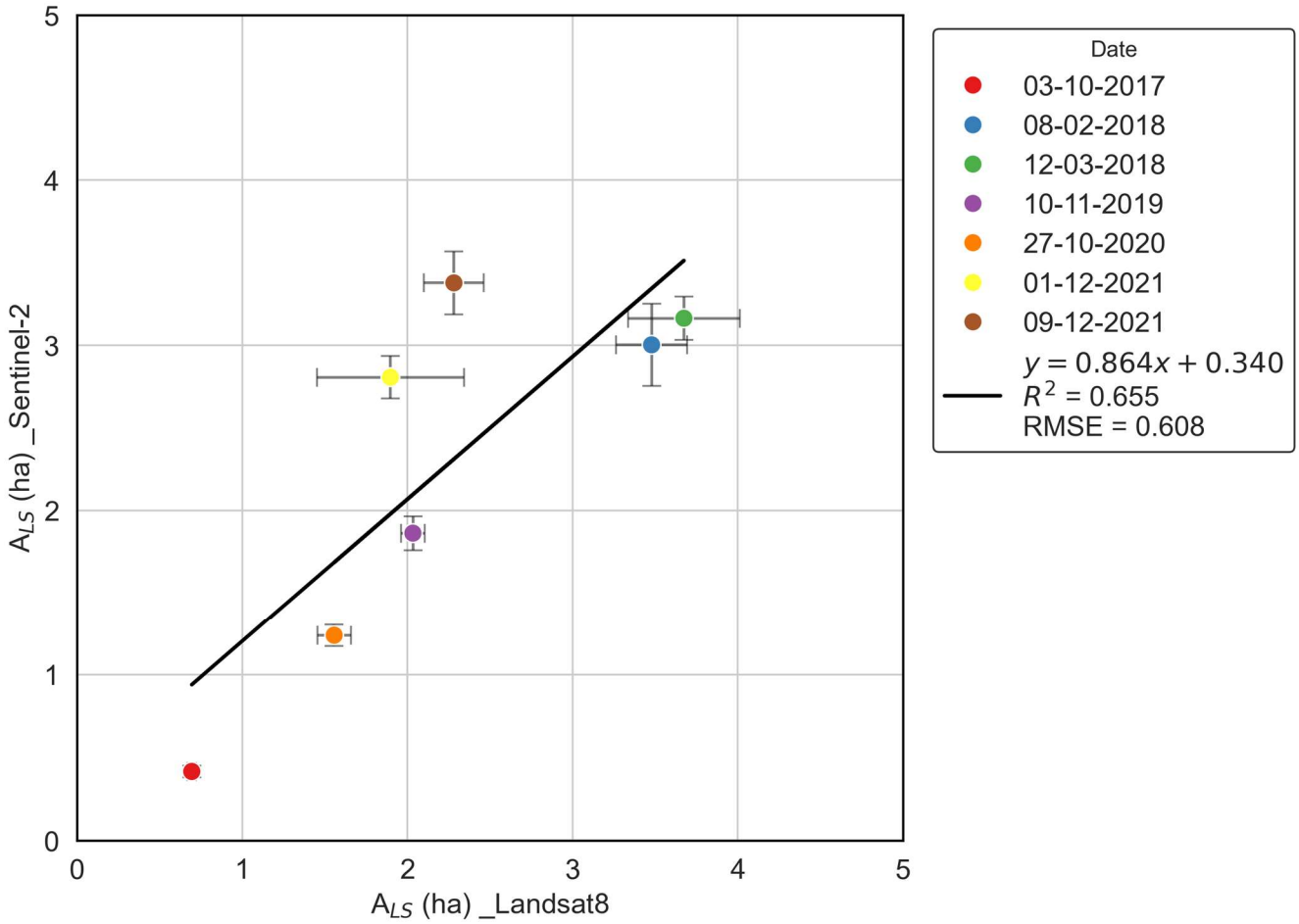

Figure C: Evaluation of resolution-induced errors using Landsat 8 and Sentinel-2 imagery

Authors' contributions. HK: Writing of the original draught and data analysis. KY: Conceptualisation, Field survey planning, Field survey, and Data analysis. SS: Aerial photogrammetry. MH: Soil sampling. SS and NB: Aerial photogrammetry. AKoyama: Field survey and Soil sampling. AKanno: Field survey. YA, MS: Field survey. All authors contributed to the interpretation of the results and the writing and editing of the final manuscript.

Competing interests. The authors declare that they have no conflict of interest.

Acknowledgements. This work was supported by JSPS KAKENHI (Grant Numbers 17H01668 and 26303015). The fieldwork was supported by staff and students from the Bengkalis State Polytechnic and the University of Riau. Particulate organic carbon analysis was performed at Saga University with the help of Prof. Yuichi Hayami and Dr. Kenji Yoshino. We also thank Editage (www.editage.jp) for the English language editing.

References

Basir, N., Hiraishi, T., and Jauhari, Z. A.: The Ability of Red Mangrove, Gray Mangrove, and Mangrove Palm to Reduce Erosion Rate at The Northern Coast of Bengkalis Island Indonesia, in: Proceedings of 11th Applied Business and Engineering Conference (ABEC 2023) (Bengkalis, Indonesia), 2023.

Bjerrum, L.: Progressive failure in slopes of overconsolidated plastic clay and clay shales. ASCE Journal of Soil Mechanics and Foundations Division, Vol. 93, SM5, 3-49, 1967.

Bowes, D.R.: A bog-burst in the Isle of Lewis. Scott. Geogr. J. 76, 21-23, 1960.

Boylan, N., Jennings, R., Long, M.: Peat slope failure in Ireland. Q. J. Eng. Geol. Hydrogeol. 41 (1), 93-108, 2008.

Brown, J., Jorgenson, M. T., Smith, O. P. and Lee, W.: Long-term rates of coastal erosion and carbon input, Elson Lagoon, Barrow, Alaska, Swets & Zeitlinger, Lisse, ISBN 90 5809 582 7, 2003.

Charity, S., Dudley, N., Oliveira, D., Stolton, S. (eds.): Living Amazon Report 2016: A Regional Approach to Conservation in the Amazon. WWF Living Amazon Initiative, Brasilia and Quito, 112, 2016.

Chambers, L. G., Steinmuller, H. E. and Breithaupt, J. L.: Toward a mechanistic understanding of "peat collapse" and its potential contribution to coastal wetland loss, Ecology, 100(7), 2019.

Chevallier, D., Glrondot, M., Péron, C., Martin, J., Bonola, M., Chevalier, J., Thoisy, B. D., Kelle, L., Maho, Y. L., Gardel, A. and Anthony, E. J.: Beach erosion aggravates the drastic decline in marine turtle populations in French Guiana, Regional Environmental Change, 23:116, 2023.

Couwenberg, J., Dommain, R., and Joosten, H.: Greenhouse gas fluxes from tropical peatlands in south-east Asia, Global Change Biology, 16, 1715–1732, 2010.

Coxon, P., Coxon, C.E., Thorn, R.H.: The Yellow River (County Leitrim, Ireland) flash flood of June 1986. In: Beven, K., Carling, P. (Eds.), Floods: Hydrological, Sedimentological and Geomorphological Implications. Wiley, Chichester, pp. 199-217, 1989.

Crisp, D.T., Rawes, M., Welch, D.: A Pennine peat slide. Geogr. J. 130 (4), 519-524, 1964.

Dariah, A., Susanti, E., Mulyani, A., and Agus, F.: Predictor factor of carbon stock in peat soils. In: Husen et al. (eds.) Sustainable Peatland Management, Indonesian Agency for Agriculture Research and Development, Ministry of Agriculture, Bogor, Indonesia, 213–221, 2012.

Day, J. W., Christian, R. R., Boesch, D. M., Yanez-Arancibia, A., Morris, J., Twilley, R. R., Naylor, L., Schaffner, L. and Stevenson, C.: Consequences of climate change on the ecogeomorphology of coastal wetlands. Estuaries and Coasts 31:477–491, 2008.

Dommain, R., Couwunberg, J., and Joosten, H.: Development and carbon sequestration of tropical peat. domes in south-east Asia: links to post-glacial sea-level changes and Holocene climate variability, Quaternary Science Reviews, 30, 999–1010, 2011.

Dugan, P.: Wetlands in Danger. Michael Beasley, Reed International Books, London. 192, 1993.

Dykes, A.P., Kirk, K.J.: Slope instability and mass movements in peat deposits. In: Martini, I.P., Martı´nez Cortizas, A., Chesworth, W. (Eds.), Peatlands: Evolution and Records of Environmental and Climatic Changes. Elsevier, Amsterdam, pp. 377-406 (Chapter 16), 2006.

Dykes P, A. and Warburton, J.: Mass movements in peat: A formal classification scheme, Geomorphology 86, 73-93, 2007.

Dykes, A.P., Warburton, J.: Geomorphological controls on failures of peat-covered hillslopes triggered by extreme rainfall. Earth Surf. Process Landforms 32, 1841-1862, 2007b.

Dykes, A.P., Jennings, P.: Peat slope failures and other mass movements in western Ireland, August 2008. Q. J. Eng. Geol. Hydrogeol. 44 (1), 5-16, 2011.

Evans, M. G. and Warburton, J.: Sediment budget for an eroding peat-moorland catchment in Northern England. Earth Surface Processes and Landforms 30(5): 557–77, 2005.

Evans, M. and Warburton, J.: Geomorphology of Upland Peat (Erosion, Form and Landscape Change), RGS-IBG book series, Blackwell Publishing, pp.262, 2007.

Frolking, S., Talbot, J., Jones, M. C., Treat, C. C., Kauffman, J. B., Tuittila, E. S., and Roulet, N.: Peatlands in the Earth of the 21st century climate system, Environmental Review, 19, 371–396, 2011.

Furmanczyk, K., and Dudzinska-Nowak, J.: Effects of extreme storms on coastline changes: a southern Baltic example. J. Coast. Res, 1637–1640, 2009.

Galy, V., Peucker-Ehrenbrink, B., and Eglinton, T.: Global carbon export from the terrestrial biosphere controlled by erosion, Nature, 521, 204–207, 2015.

Harper, J.R.: Coastal erosion rates along the Chucki Sea coast near Barrow, Alaska, Arctic 31: 428–433, 1978.

Hedges, J.I., Quay, P.D., Grootes, P.M., Richey, J.E., Devol, A.H., Farwell, G.W., Schmidt, F.W., and Salati, E.: Organic Carbon-14 in the Amazon River system: Science, v.231, 1129–1131, 1986.

Hedges, J.I. and Keil, R.G.: Sedimentary organic matter preservation: an assessment and speculative synthesis, Marine Chemistry, 49, 81–115, 1995.

Hilton, R. G., Galy, V., Gaillardet, J., Dellinger, M., Bryant, C., O'Regan M., Gröcke, D.R., Coxall, H., Bouchez, J., and Calmels, D.: Erosion of organic carbon in the Arctic as a geological carbon dioxide sink, Nature, 524, 84-87, 2015.

Hirano, T., Segah, H., Harada, T., Limin, S., June, T., Hirata, R., and Osaki, M.: Carbon dioxide balance of a tropical swamp forest in Kalimantan, Indonesia, Global Change Biology, 13, 412–425, 2007.

Hirano, T., Segah, H., Kusin, K., Limin, S., Takahashi, H., and Osaki, M.: Effects of disturbances on the carbon balance in tropical peat swamp forests, Global Change Biology, 18, 3410–3422, 2012.

Hirano, T., Kusin, K., Limin, S., and Osaki, M.: Carbon dioxide emissions through oxidative peat decomposition on burnt tropical peatland, Global Change Biology, 20, 555–565, 2014.

Hooijer, A., Page, S., Canadell, J. G., Silvius, M., Kwadijk, J., Wösten, H., and Jauhiainen, J.: Current and future CO_2 emissions from drained peatlands in Southeast Asia, Biogeosciences, 7, 1505–1514, 2010.

Hume, J.D. and Schalk, M.: Shoreline processes near Barrow, Alaska: a comparison of the normal and the catastrophic, Arctic 20: 86–103, 1967.

Hume, J.D., Schalk, M. and Hume, P.W.: Short-term climate changes and coastal erosion, Barrow, Alaska, Arctic 25: 272–278, 1972.

Hussein, A. H.: Modeling of sea-level rise and deforestation in submerging coastal ultisols of Chesapeake Bay. Soil Science Society of America Journal 73:185–196, 2009.

IPCC. 2007. Climate change 2007: the physical science basis: contribution of working group I to the fourth assessment report of the intergovernmental panel on climate change. S. Solomon, D. Qin, M. Manning, Z. Chen, M. Marquis, K. B. Averyt, M. Tignor, and H. Miller, editors. Cambridge University Press, Cambridge, UK, 2007.

Kagawa, H., Yamamoto, K., Haidar, M., Kanno, A., Akamatsu, Y., Suzuki, M., Sutikno, S., Basir, N., and Sekine, M.: Present condition of coastal erosion in the Islands in Riau Province, Indonesia, in: Proceedings of the Civil Engineering Society G (Environment) (Collection of Research Papers on Environmental Engineering), 73(7), III_213–III_219, 2017.

Kirk, K.J.: Instability of Blanket Bog Slopes on Cuilcagh Mountain, N.W. Ireland (Unpublished Ph.D. thesis). University of Huddersfield, U.K, 2001.

Kleinen, T., Brovkin, V., von Bloh, W., Archer, D., and Mun-hoven, G.: Holocene carbon cycle dynamics, Geophysical Research Letters, 37, L02705, 2010.

Koyama, A., Yamamoto, K., Sutikno, S., Basir, N., and Suzuki, M.: Investigaiton of Peat Landslide in Indonesia Bengkalis Island by Sounding Test, in: Proceedings of 53rd Geotechnical Engineering Research Meeting (Takamatsu City), 2018.

Krauss, K. W., Cahoon, D. R., Allen, J. A., Ewel, K. C., Lynch, J. C., and Cormier, N.: Surface elevation change and susceptibility of different mangrove zones to sea-level rise on Pacific high islands of Micronesia. Ecosystems 13:129–143, 2010.

Kreuzburg, M., Ibenthal, M., Janssen, M., Rehder, G., Voss, M., Naumann, M. and Feldens, P.: Sub-marine Continuation of Peat Deposits from a Coastal Peatland in the Southern Baltic Sea and its Holocene Development, Frontiters in Earth Sciences, Volume6, Article103,1-12, 2018.

Lantuit H. and Pollard W.H.: Fifty years of coastal erosion and retrogressive thaw slump activity on Herschel Island, southern Beaufort Sea, Yukon Territory, Canada, Geomorphology 95, 84-102, 2008.

Lantuit, H., Atkinson, D., Overduin, P. P., Grigoriev, M., Rachold, V., Grosse, G. and Hubberten, H. W.: Coastal erosion dynamics on the permafrost-dominated Bykovsky Peninsula, north Siberia, 1951-2006, Polar Research, 30:1, 7341, 2011.

Lehfeldt, R., and Milbradt, P.: "Longshore sediment transport modelling in 1 and 2 dimensions, in: advances in Hydro-science and engineering," in: Proceedings of the 4th International Conference on Hydro-Science and Engineering Abstract (Seoul), 2000.

Ludwig, W.., Probst, J. L., and Kempe, S.: Predicting the oceanic input of organic carbon by continental erosion, Global Biogeochemical Cycles, 10(1), 23–41, 1996.

MacCarthy, G.R.: Recent changes in the shoreline near Point Barrow Alaska, Arctic 6: 44–51, 1953.

Mandanici, E. and Bitelli, G.: Preliminary Comparison of Sentinel-2 and Landsat 8 Imagery for a Combined Use, Remote sensing, 8, 1014, 1-10, 2016.

Malpica-Piñeros, C., Barthelmes, A. and Joosten, H.: What, when and how? A review of peatland research in Amazonia, Mires and Peat, Volume 31, Article 03, 26, 2024.

Mariotti, G., and Fagherazzi, S.: A numerical model for the coupled long-term evolution of salt marshes and tidal flats, Journal of Geophysical Research: Earth Surface 115:1–15, 2010.

Mayorga, E., Aufdenkampe, A.K., Masiello, C.A., Krusche, A.V., Hedges, J.I., Quay, P.D., Richey, J.E., and Brown, T.A.: Young organic matter as a source of carbon dioxide outgassing from Amazonian rivers, Nature, v.436, 538–541, 2005.

McCahon, C.P., Carling, P.A., Pascoe, D.: Chemical and ecological effects of a Pennine peat-slide. Environ. Pollut. 45, 275-289, 1987.

Mills, A.J., 2002. Peat Slides: Morphology, Mechanisms and Recovery (Unpublished Ph.D. thesis). University of Durham, UK, 2002.

Ministry of the Environment White Paper, Introduction, Section 1, Subsection 2: Global Environment, 2002.

Nicholls, R. J., Hoozemans, F. M. J. and Marchand,M.: Increasing flood risk and wetland losses due to global sea-level rise: regional and global analyses. Global Environmental Change—Human and Policy Dimensions 9: S69–S87, 1999.

Osaki, M. and Tsuji, N.: Tropical peatland ecosystems, Springer Tokyo, 633pp, 2016.

Page, S.E., Siegert, F., Rieley, J.O., Boehm, H.D.V., Jaya, A., and Limin, S.: The amount of carbon released from peat and forest fires in Indonesia during 1997, Nature, 420, 61–65, 2002.

Page, S.E., Rieley, J., and Banks, C.: Global and regional importance of the tropical peatland carbon pool, Global Change Biology, 17, 798–818, 2011.

Rachold, V., Brown, J. and Solomon, S. (eds).: Arctic Coastal Dynamics-Report of an International Workshop, Reports on Polar and Marine Research, 413, 103, 2002.

Richey, J.E., Melack, J.M., Aufdenkampe, A.K., Ballester, V.M., and Hess, L.L.: Outgassing from Amazonian rivers and wetlands as a large tropical source of atmospheric CO_2, Nature, v.416, 617–620, 2002.

Ritung, S., Wahyunto, Nugroho, K., Sukarman, Hikmatullah, Suparto, and Tafakresnanto, C.: Tim Penyusun Peta Lahan Gambut Indonesia Skala 1:250.000 (Indonesian peatland map at the scale 1:250,000), Indonesian Center for Agricultural Land Resources Research and Development, Bogor, Indonesia, 2011.

Rudiyanto, Minasny, B., Satyanto, B.I., Saptomo, S.K., and McBratney, A.B.: Open digital mapping as a cost-effective method for mapping peat thickness and assessing the carbon stock of tropical peatlands, Geoderma, 313, 25–40, 2018.

Scharlemann, J. P., Tanner, E. V., Hiederer, R. and Kapos, V.: Global soil carbon: understanding and managing the largest terrestrial carbon pool, Global soil carbon: understanding and managing the largest terrestrial carbon pool, Carbon Management, 5:1, 81-91, 2014.

Schwimmer, R.: Rates and processes of marsh shoreline erosion in Rehoboth Bay, Delaware, USA. Journal of Coastal Research 17:672–683, 2001.

Supardi, Subekty, A.D., and Neuzil, S.G.: General geology and peat resources of Siak Kanan and Bengkalis Island peat deposits, Sumatra, Indonesia, Geological Society of America Special Paper, 286, 45–61, 1993.

Sutikno, S., Sandhyavitri, A., Haidar, M., and Yamamoto, K.: Shoreline Change Analysis of Peat Soil Beach in Bengkalis Island Based on GIS and RS, International Journal of Engineering and Technology. 9, 3, 233–238, 2017.

Umarhadi. D. A., Widyatmanti, W., Kumar, P., Yunus, A. P., Khedger, K. M.., Kharazi, A., and Avtar, R..: Tropical peat subsidence rates are related to decadal LULC changes: Insights from InSAR analysis, Science of the Total Environment, 816, 151561, 2022.

US Army Map Service: Bengkalis, Series T503, NA48-9, 1955.

Vestergaard, P.: Possible impact of sea-level rise on some habitat types at the Baltic coast of Denmark. J. Coast. Conserv. 3, 103, 1997.

Wahyunto, Ritung, S., and Subagjo, H.: Peta Luas Sebaran Lahan Gambut dan Kandungan Karbon di Pulau Sumatera / Maps of Area of Peatland Distribution and Carbon Content in Sumatra: 1990–2002, Wetlands International—Indonesia Programme & Wildlife Habitat Canada (WHC), Bogor, Indonesia, 2003.

Warburton, J., Holden, J., and Mills, A.J.: Hydrological controls of surficial mass movements in peat, Earth-Science Reviews, 67, 139–156, 2004.

Warren, M.W., Kauffman, J.B., Murdiyarso, D., Anshari, G., Hergoualc'h, K., Kurnianto, S., Purbopuspito, J., Gusmayanti, E., Afifudin, M., Rahajoe, J., Alhamd, L., Limin, S., and Iswandi, A.: A cost-efficient method to assess carbon stocks in tropical peat soil, Biogeosciences, 9, 4477–4485, 2012.

Wilford, G. E.: Peat landslide in Sarawak, Malaysia, and its significance in relation to washouts in coal seams, Journal of sedimentary Research, 36(1), 244 247, 1966.

Wilson, P., Griffiths, D., Carter, C.: Characteristics, impacts and causes of the Carntogher bog-flow, Sperrin Mountains, Northern Ireland. Scott. Geogr. Mag. 112, 39-46, 1996.

Wong, P. P., Losada, I. J., Gattuso, J.-P., Hinkel, J., Khattabi, A., McInnes, K. L., et al.: Coastal systems and low-lying areas. Clim. Change 2104, 361–409, 2014.

Xu, J., Morris, P.J., Liu, J., and Holden, J.: PEATMAP: Refining estimates of global peatland distribution based on meta-analysis. University of Leeds. Online at https://doi.org/10.5518/252, accessed January 18, 2024, 2017.

Yamamoto, K., Asakuma, T., Kagawa, H., Sutikno, S., Basir, N., and Kanno, A.: Occurrence and disappearance of temporary peat fan by the landslide at the coastal peat coast, in: Proceedings of the Civil Engineering Society B2 (Coastal Engineering) 75(2): I _1249–I _1254, 2019.

Yamamoto, K., Basir, N., Sutikno, S., Kanno, A., Kagawa, H., Suzuki, M., Akamatsu, Y., and Koyama, A.: Tropical peat debris storage in the tidal flat in northern Bengkalis Island, Indonesia, in: Proceedings of MATEC Web of Conferences, 276, 06002, 2019.

Yamamoto, K., Watanabe, M., Kagawa, H., Matsumoto, A., Sutikno, S., and Koyama, A.: Elution of dissolved organic matter into coastal seawater from collapsed peat deposit, in: Proceedings of the Civil Engineering Society B2 (Coastal Engineering), 76(2), I_1333–I_1338, 2020.

Yu, Z.: Holocene carbon flux histories of the world's peatlands: global carbon cycle implications, The Holocene, 21(5), 761–774, 2011.

Yunker, M. B., Macdonald, R. W., Fowler, B. R., Cretney, W. J., Dallimore, S. R. and Mclaughlin, F. A.: Geochemistry and fluxes of hydrocarbons to the Beaufort Sea shelf: A multivariate comparison of fluvial inputs and coastal erosion of peat using principal components analysis, Geochimica et Cosmochimica Acta Vol.55, 255-273, 1991.